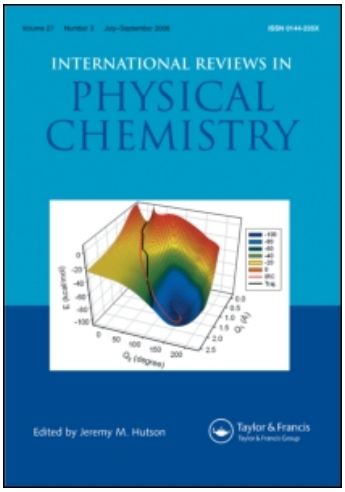

International Reviews in Physical Chemistry
Publication details, including instructions for authors and subscription information:
http://www.informaworld.com/smpp/title~content=t713724383

Crossed molecular beam reactive scattering: from simple triatomic to multichannel polyatomic reactions

Nadia Balucani[a]; Giovanni Capozza[a]; Francesca Leonori[a]; Enrico Segoloni[a]; Piergiorgio Casavecchia[a]
[a] Dipartimento di Chimica, Università degli Studi di Perugia, 06123 Perugia, Italy

Online publication date: 28 November 2010

To cite this Article Balucani, Nadia , Capozza, Giovanni , Leonori, Francesca , Segoloni, Enrico and Casavecchia, Piergiorgio(2006) 'Crossed molecular beam reactive scattering: from simple triatomic to multichannel polyatomic reactions', International Reviews in Physical Chemistry, 25: 1, 109 — 163
To link to this Article: DOI: 10.1080/01442350600641305
URL: http://dx.doi.org/10.1080/01442350600641305

International Reviews in Physical Chemistry,
Vol. 25, Nos. 1–2, January–June 2006, 109–163

Taylor & Francis
Taylor & Francis Group

Crossed molecular beam reactive scattering: from simple triatomic to multichannel polyatomic reactions

NADIA BALUCANI, GIOVANNI CAPOZZA, FRANCESCA LEONORI, ENRICO SEGOLONI and PIERGIORGIO CASAVECCHIA*

Dipartimento di Chimica, Università degli Studi di Perugia, 06123 Perugia, Italy

(*Received 31 January 2006; in final form 13 February 2006*)

In our laboratory a recent series of experiments by means of the crossed molecular beam (CMB) scattering technique with mass-spectrometric detection and time-of-flight analysis has been instrumental in fostering progress in the understanding of the dynamics of both simple triatomic *insertion* reactions and complex polyatomic *addition–elimination* reactions exhibiting competing channels. In the first part of this review we survey the advances made in the comprehension of the dynamics of the *insertion* reactions involving excited carbon, nitrogen and oxygen atoms – $C(^1D)$, $N(^2D)$, $O(^1D)$ – with $H_2(D_2)$, as made possible by synergistic comparisons of experimental reactive differential cross-sections with the results of exact quantum, quasiclassical trajectory and statistical calculations on reliable *ab initio* potential energy surfaces. Related experimental and theoretical work from other laboratories is noted throughout. In the second part, we review the progress made in the understanding of the dynamics of polyatomic multichannel reactions, such as those of ground state oxygen and carbon atoms, $O(^3P)$ and $C(^3P)$, with the simplest alkyne, acetylene, and alkene, ethylene, as made possible by the gained capability of identifying virtually all primary reaction channels, characterising their dynamics, and determining their branching ratios. Such a capability is based on an improved crossed molecular beam instrument which features product detection by low-energy electron soft-ionisation for increased sensitivity and universal detection power, and variable beam crossing angle for a larger collision energy range and increased angular and velocity resolution. The scattering results are rationalised with the assistance of theoretical information from other laboratories on the stationary points and product energetics of the relevant *ab initio* potential energy surfaces. These detailed studies on polyatomic multichannel reactions provide an important bridge between crossed beam dynamics and thermal kinetics research.

Contents

*Corresponding author. Email: piero@dyn.unipg.it

International Reviews in Physical Chemistry
ISSN 0144–235X print/ISSN 1366–591X online
http://www.tandf.co.uk/journals
DOI: 10.1080/01442350600641305

1. Introduction

A fundamental goal of physical chemistry is to understand how chemical reactions occur at the microscopic level. This is the realm of *reaction dynamics*, a branch of physical chemistry/chemical physics which is nowadays one of the major patterns of enquiry in chemical kinetics. In an ideal experiment of reaction dynamics, collisions involving reactants with well-defined internal states and relative velocity are investigated and the products fully characterised. Fundamental questions on the evolution from reactants to products can therefore be addressed, especially when direct comparisons with scattering calculations on accurate potential energy surfaces (PESs) are available. Indeed, pivotal to the strong progress that has occurred in the field of reaction dynamics over the past 50 years has been the strong synergistic interplay between experiment and theory.

From an experimental point of view, crossed molecular beams (CMB) methods are particularly powerful for investigating gas-phase reaction dynamics [1–5]. The basic characteristics of CMB experiments with respect to bulk and pump–probe time-resolved flow studies is that the reactants are confined into distinct supersonic beams which cross each other at a specific angle; the species of each beam are characterised by a well-defined (both in magnitude and direction) velocity and usually also internal quantum states, and are made to collide only with the molecules of the other beam, allowing us to observe the consequences of well-defined molecular collisions. Product detection in

CMB experiments can be performed by mass spectrometry or laser spectroscopy. The CMB technique with electron-ionisation (EI) mass-spectrometric detection was first developed in the late 1960s [6] and, since then, it has continuously evolved [1, 2, 7–13]. Using this technique in its 'classic' version [1], product angular and velocity distributions (i.e. the double differential cross-sections, DCSs) can be measured at well-defined collision energies (i.e. relative translational energies), E_c; usually, total (i.e. summed over all product internal quantum states) DCSs are determined, and in some favourable cases vibrationally resolved DCS can also be obtained [7, 9]. This technique has been central in the investigation of the dynamics of bimolecular reactions during the past 35 years [14–16]. In CMB experiments product detection can also be accomplished by means of LIF (Laser Induced Fluorescence) within Doppler-shift schemes [17–20] or, more efficiently, by REMPI (Resonant Enhanced Multiphoton Ionization) which can be optimally coupled with ion-imaging [21–31], or by the H-atom Rydberg tagging time-of-flight (TOF) technique [32–38]. Vibrationally and also rotationally resolved DCSs can be measured using these high-resolution pulsed CMB/laser techniques.

During the past 10–15 years, by exploiting the classic CMB method and CMB/laser techniques, it has been possible to carry out very detailed measurements of (state-to-state) integral and differential cross-sections for simple triatom ($H + H_2$, $F + H_2$, $Cl + H_2$) and a four-atom ($OH + H_2$) bimolecular *abstraction* reactions, and these experimental quantities have been the subject of very detailed comparisons with theoretical predictions based on both exact quantum-mechanical (QM) and quasiclassical trajectory (QCT) scattering calculations on *ab initio* PESs. All this has permitted us to deepen significantly our understanding of abstraction reactions [14, 19, 20, 27, 32–34, 37–49]. More recently, detailed combined experimental and theoretical investigations have also been extended to encompass another category of triatom reactions, the so-called *insertion* reactions, such as those between an electronically excited atom – $C(^1D)$, $N(^2D)$, $O(^1D)$ or $S(^1D)$ – and molecular hydrogen. A variety of studies using the classic CMB method in our laboratory [50–58] and CMB/laser techniques in other laboratories [35, 36, 59–63], have provided a wealth of experimental information on these reactions. The experimental studies have been again accompanied by synergistic theoretical efforts both at the level of *ab initio* electronic structure calculations of the PESs and of dynamics calculations (QM, QCT and statistical) (see section 3). The first part of this review (section 3) will survey the progress recently made in our laboratory in the understanding of three simple *insertion* reactions. We will see that our results and related work from other laboratories have permitted us to learn a lot also about this reaction mechanism which, together with *abstraction* and *addition–elimination*, is one of the most common mechanisms in chemistry.

Besides fundamental aspects, reaction dynamics studies have also addressed important issues in applied areas, such as combustion, atmospheric chemistry and astrochemistry. In these environments most reactions encompass polyatomic molecules or radicals as reactants/products, and usually involve several energetically allowed product channels. A full characterisation of these systems is therefore much more challenging than in the case of simple triatom reactions. For polyatomic multichannel reactions one would like to be able to determine for each channel (i) the primary products, (ii) its relative importance, and (iii) its mechanism. This goal is very difficult to achieve by using any of the several high-resolution laser-based spectroscopic

techniques commonly used for reaction dynamics studies at the state-resolved level. This is because products often are not known or include polyatomic radicals whose spectroscopy is not known or for which suitable LIF or REMPI schemes or laser sources are not available. An example in which spectroscopic techniques might work well is represented by the recent studies on the dynamics of chlorine atom reactions with polyatomic organic molecules; in these systems the Cl-atom abstracts an H-atom leading to the formation of HCl plus an organic radical, and the HCl product is ideally detected by REMPI spectroscopy. An excellent review has recently been published on these studies [64, 65]. Other examples exploit a very recent experimental set-up, based on pulsed CMB experiments coupled to a novel time-sliced ion velocity imaging technique for the measurements of the velocity distribution of a state-selected product by REMPI [21–27]. This has permitted determining integral and double differential cross-sections at the state-resolved level by detecting CH_3 for the family of polyatomic *abstraction* reactions $X + CH_4 \rightarrow CH_3\ (v) + HX\ (v)$ (X = F, Cl, O, OH) (and their isotopomers). The approach is analogous to the one previously used for triatom systems as $F + H_2 \rightarrow H + HF\ (v)$, but with the additional feature of pair-correlated information on the DCSs for the two product partners, thus providing unprecedented, detailed insight on polyatomic reactions [21–27].

Elegant as those experiments are, they remain confined to the study of reactions forming very few simple species. Undoubtedly, the technique most versatile to tackle polyatomic multichannel reactions is the classic CMB scattering technique with *universal* EI mass spectrometric detection and TOF analysis. In principle this method permits one to identify unambiguously all the primary products (even when their nature is unknown), determine the product energy partitioning between translation and internal degrees of freedom, derive the product angular distributions in the centre-of-mass system and obtain information on the micromechanism of the reaction. Ultimately one can derive information on some important features of the underlying PES. By using this technique, during the last decade we have investigated a series of complex polyatomic reactive systems such as $C(^3P) + C_2H_2$ [66–68], $C(^3P) + C_2H_4$ [69], $N(^2D) + CH_4$ [66, 70], $N(^2D) + C_2H_2$ [71], $N(^2D) + C_2H_4$ [72], $N(^2D) + H_2O$ [66, 73], $O(^3P,^1D) + H_2S$ [8, 74], and $O(^3P,^1D) + CH_3I$ [75]. A very comprehensive review on reaction dynamics with molecular beams, which includes CMB and CMB/laser studies of simple reactions and CMB studies of polyatomic reactions, was published about six years ago [14]. It should be noted that until that time, and actually until a couple of years ago, despite the universal detection capabilities of the classic CMB method, only one or very few reaction channels of a polyatomic reaction could be investigated because of some limitations of the method, most notably connected with the dissociative ionisation effects (see section 2). An exception is represented by a series of CMB studies on a number of reactions of $O(^1D)$ atoms with saturated hydrocarbons and various molecules where, by exploiting isotopically labelled ^{18}O beams, it has been possible to detect all product channels [16].

In the last few years, to reduce the problem of dissociative ionisation we have successfully implemented the soft electron-ionisation (EI) technique for product detection, a novel experimental strategy in CMB experiments [2, 76, 77]. This has proved to be essential for characterising virtually all the competing pathways of multichannel reactions, enabling us to explore the dynamics of polyatomic reactive

systems more comprehensively than previously possible. The second part of this review (section 4) will survey our recent progress in the investigation of the dynamics of some multichannel polyatomic reactions of ground state O and C atoms with unsaturated hydrocarbons, as made possible by the application of the soft EI detection method in CMB reactive scattering experiments, as well as of the new capability of crossing the two reactant beams at angles both smaller (45°) and larger (135°) than the common 90°.

Before reviewing the above topics, we will recall the basics of the CMB technique and outline the improvements brought to our CMB instrument that have determined a new twist on reactive scattering studies of polyatomic reactions.

2. Experimental: improved crossed molecular beams apparatus

The principles of CMB reactive scattering experiments with mass spectrometric detection and TOF analysis have been discussed at length in reviews and book chapters [1, 8, 14]. Briefly, in the typical arrangement of a CMB apparatus (see figure 1), two

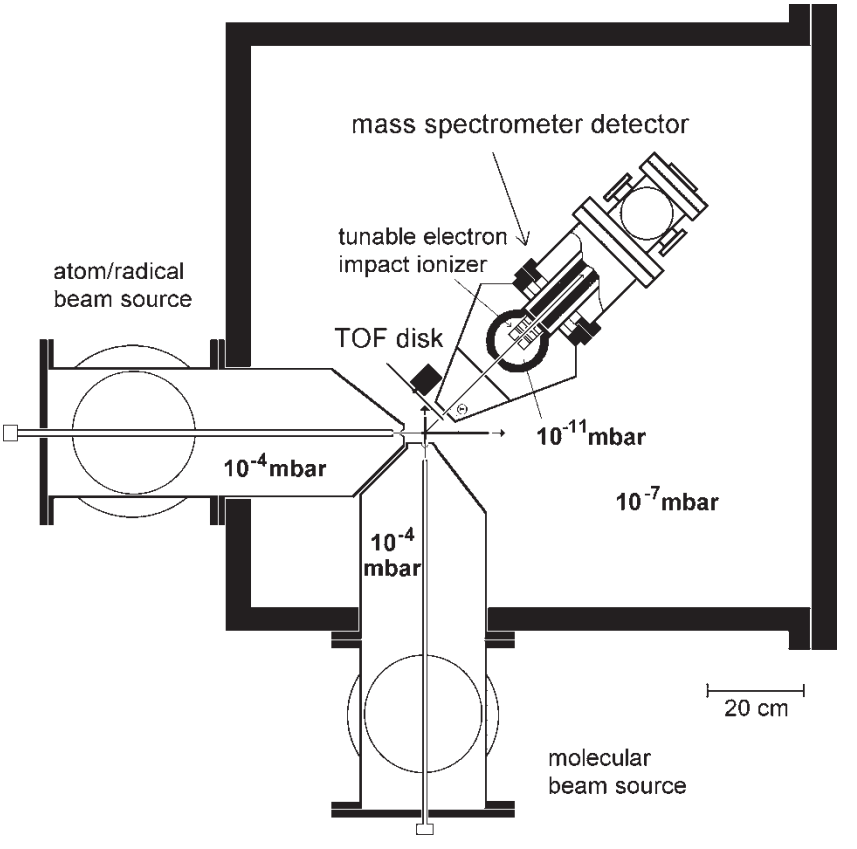

Figure 1. Schematic view of the 'classic' crossed molecular beams apparatus of Perugia with rotating TOF mass spectrometer detector and 90° beam crossing angle geometry.

beams of atoms and molecules with narrow angular and velocity spread are crossed at 90° in a high-vacuum chamber and the angular and TOF distributions of the products are recorded after well-defined collisional events take place. The detector is usually an electron-impact ioniser followed by a quadrupole mass filter; the whole detector unit can be rotated in the collision plane around the axis passing through the collision centre. The main aspects of our CMB machine have been described in detail elsewhere [8, 14]; here, we will mainly describe the recent improvements of the experimental set-up, namely the implementation of the soft electron-ionisation for product detection and the new arrangement of variable crossing angle of the two reactant beams.

2.1. *Soft electron-ionization detection*

The use of electron-ionisation mass-spectrometric detection renders the CMB method *universal*, that is applicable in principle to the study of any reaction. Every species can, in fact, be ionised at the typical electron energy used in the ioniser which precedes the mass filter of the detector [6, 8, 11]. Since the introduction of the technique in 1969 [6], because of the very low number density of products to be detected in these experiments, a high electron energy of 60–200 eV (hard ionisation) had to be used for product ionisation in order to maximise the signal. Most neutral species, in fact, have the maxima of their EI cross-section at ~70 eV. Unfortunately hard EI is plagued by the problem of the dissociative ionisation, which constitutes the most serious limit with the mass spectrometric detection in CMB experiments [1, 10]. This phenomenon is well known. In analytical chemistry it is often exploited to recognize complex molecules from their fragmentation patterns, but in CMB experiments it represents a very serious complication. This is especially true when the signal at a certain mass-to-charge ratio (m/z) can originate from more than one product. For instance, this is a common situation for reactions producing organic radicals/molecules because of their tendency to fragment in the ioniser. Only in favourable cases is it possible to distinguish whether an ion at a given m/z originates from different neutral products by exploiting energy and momentum conservation (ion fragments coming from the same product will exhibit identical angular and velocity distributions) [1]. Especially troublesome is the case in which the reactants themselves can interfere with product detection. For instance, it would be practically impossible to detect any of the two co-products originating from:

$$C(^3P) + C_2H_4 \rightarrow CH_2 + C_2H_2 \quad \Delta H_0^\circ = 142\,\mathrm{kJ\,mol^{-1}}$$

which is an energetically allowed channel of the reaction between atomic carbon and the ethylene molecule [69]. In fact, the reactive scattering signal at $m/z = 14$ (CH_2) or 26 (C_2H_2) would be overwhelmed, when using hard EI, by the much more intense signal (by nearly two orders of magnitude) at these masses originating from dissociative ionisation of *elastically/inelastically* scattered C_2H_4 (see section 4.4.2).

An elegant way to overcome this problem was prompted by Nobel Laureate Y. T. Lee who introduced, during the mid-1990s, the soft (i.e. non-dissociative) photo-ionisation (PI) method by tunable VUV radiation from a third-generation synchrotron

(such as the Advanced Light Source, ALS, in Berkeley), capable of delivering a flux of 10^{16} photons s^{-1}, mandatory for reactive scattering experiments [10]. More recently, this approach has also been implemented in Taiwan [78–80]. By using tunable (5–30 eV) quasicontinuous VUV synchrotron radiation, and by tuning the photon energy below the threshold for dissociative ionisation of interfering species, one can often eliminate background signal that would normally prohibit experiments using hard EI [78–81]. A remaining problem is the low ionisation efficiency, PI cross-sections being typically about one–two orders of magnitude smaller than EI cross-sections. A variety of photodissociation studies in recent years have demonstrated the power of soft PI by synchrotron radiation [78–86], but there have been only very few examples of reactive scattering studies exploiting this approach, namely those on the reactions Cl + propane and n-pentane [87–89].

Following a similar idea, single photon PI by a 157 nm F_2 laser (7.9 eV radiation) has been recently used in reactive scattering studies of transition metals, exploiting the low ionisation potentials of these metals and their compounds [13, 90–92]. Obviously this detection approach remains confined, beyond transition metal compounds, to a limited number of large polyatomic radicals having an ionization energy somewhat below 7.9 eV.

Notwithstanding the success of those experiments, a shortcoming with the VUV PI approach is that absolute PI cross-sections are very often not known, and therefore branching ratios cannot be easily estimated. As a matter of fact, studies of photodissociation processes by soft PI using synchrotron light are usually accompanied by measurements carried out using *hard* EI, where many data have to be taken at all possible fragment masses in order to estimate branching ratios [78–80, 82–86].

In our laboratory, we have very recently implemented in CMB reactive scattering experiments an alternative method, that is, product detection by soft EI, which is achieved by using electrons with low, tunable energy [12]. Although not affording the same degree of selectivity as VUV synchrotron radiation, the soft EI approach offers similar advantages with respect to the dissociative ionisation problem; in addition, it gives us the bonus of the possibility of determining branching ratios, since absolute EI cross-sections are often known or can be reliably estimated [86, 91–93]. The soft EI approach is well known in mass spectrometry and widely used, for instance, in discharge-flow mass-spectrometric kinetic studies, but it was never applied in CMB experiments prior to our recent work [76, 77], mainly because of the low detection sensitivity. In fact, the method involves varying the energy of the ionising electrons down to low values and it is well known that EI cross-sections decrease dramatically towards threshold, leaving usually no sufficient signal for carrying out product angular and velocity distribution measurements. However, as we all know, it is all a matter of signal-to-noise ratio! Exploiting some experimental improvements which have led to an increased sensitivity of the CMB instrument [12], we have recently shown [76, 77] that the simple approach of soft EI permits in many cases to achieve *universal* detection in CMB experiments, and thus to identify all primary reaction products of multichannel reactions, determine their branching ratios, and characterise the reaction dynamics of each channel (see section 4). Because of its simplicity and low cost, the soft EI method certainly represents an attractive alternative to the use of soft PI by synchrotron radiation.

2.2. *Product angular and velocity distributions*

The quantities which are measured in a CMB experiment with mass spectrometric/TOF detection are the product intensity as a function of the scattering angle, what we call the laboratory angular distribution, $N(\Theta)$, and the product intensity as a function of the scattering angle Θ and arrival time t, what we call the time-of-flight spectrum, $N(\Theta, t)$. The measurements are carried out in the laboratory (LAB) system of coordinates, but for the physical interpretation of the scattering data it is necessary to perform a coordinate transformation and move to the centre-of-mass (CM) reference frame [1]. It can be easily demonstrated [1] that, for each reaction channel, the relation between LAB and CM product flux is given by $I_{LAB}(\Theta, v) = I_{CM}(\theta, u)v^2/u^2$, where Θ and v are the LAB scattering angle and velocity, respectively, while θ and u are the corresponding CM quantities (see the velocity vector, or 'Newton', diagram in figure 2). Since the EI mass-spectrometric detector measures the number density of products, $N(\Theta)$, rather than the flux, the actual relation between the LAB density and the CM flux is given by $N_{LAB}(\Theta, v) = I_{CM}(\theta,u)\,\frac{v}{u^2}$.

Because of the finite resolution of experimental conditions (angular and velocity spread of the reactant beams and angular resolution of the detector), the LAB to CM transformation is not single-valued and, therefore, analysis of the laboratory data is usually performed by forward convoluting tentative CM distributions over the experimental conditions. In other words, the CM angular and velocity distributions are assumed, averaged and transformed to the LAB frame for comparison with the experimental distributions and the procedure is repeated until a satisfactory fit of the experimental distributions is obtained. The final outcome of a reactive scattering experiment is the generation of a velocity flux contour map of the reaction products for each channel, i.e. the plot of intensity as a function of angle and velocity in the CM system, $I_{CM}(\theta, u)$. The differential cross-section $I_{CM}(\theta, u)$ is commonly factorised into the product of the velocity (or translational energy) distribution, $P(u)$ (or $P(E_T')$), and the angular distribution, $T(\theta)$:

$$I_{CM}(\theta, E_T') = T(\theta)P(E_T')$$

In some cases the coupling between the $T(\theta)$ and $P(E_T')$ functions needs to be accounted for (see section 3.1). The $T(\theta)$ and $P(E_T')$ functions contain all the information about the dynamics.

When multiple reaction channels contribute to the signal at a given m/z ratio, a more complex situation arises. For instance, figure 2 is shows the Newton diagram for an experiment where a typical atomic beam of species A crosses at 90° a hydrocarbon beam of species RR′H (where R is a hydrocarbon radical and R′ is either an H atom or another hydrocarbon radical) and reacts according to the generic scheme:

$$\begin{aligned} A + RR'H &\rightarrow RR'A + H \\ &\rightarrow RA + R'H \end{aligned}$$

By taking into account the reactant and product masses and the laws of conservation of linear momentum and total energy, it is possible to calculate the maximum CM speed that the products can reach and therefore to draw the limiting circles in the Newton diagram which define the range of LAB angles within which the products can be scattered. By setting the mass spectrometer detector at the m/z ratio of the parent ion

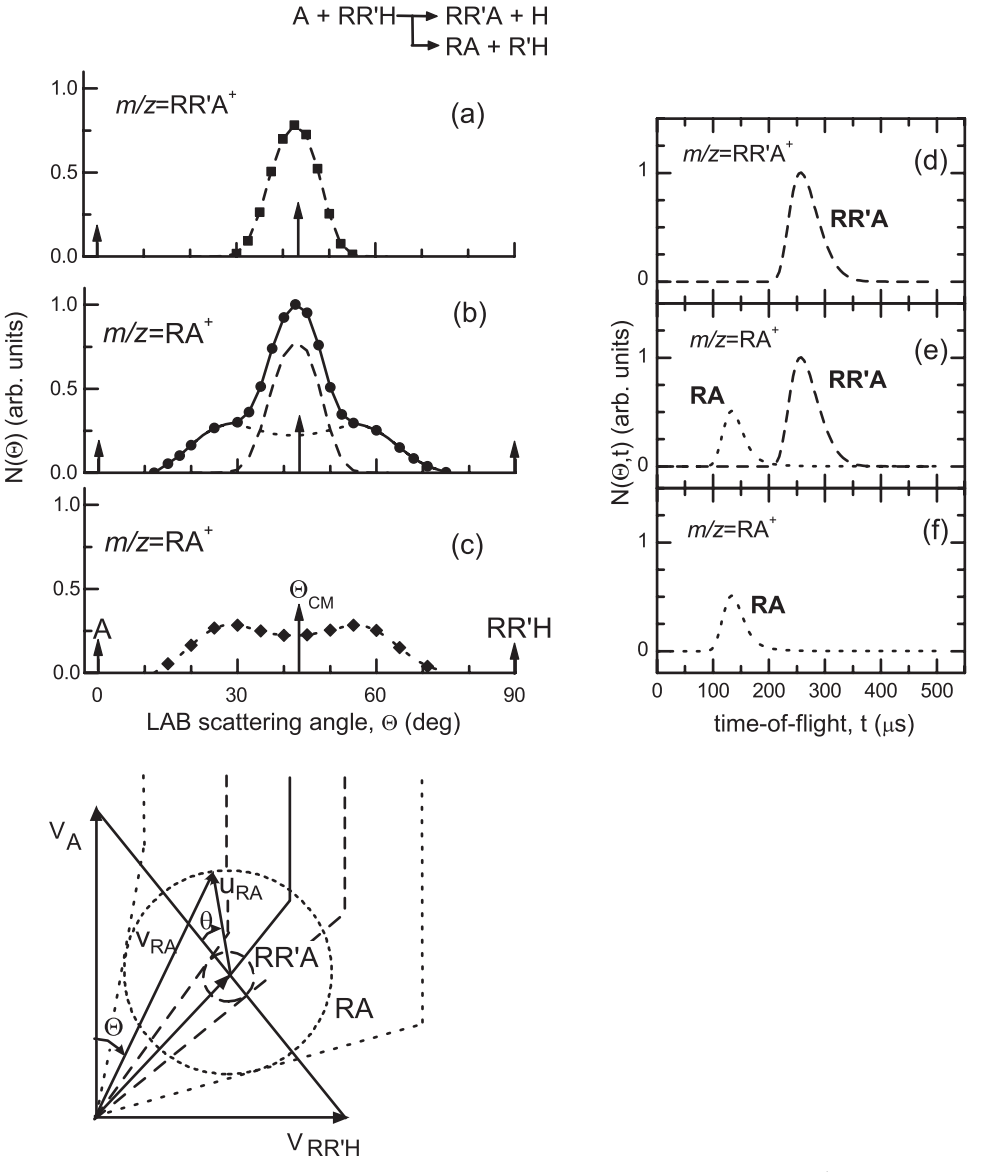

Figure 2. LAB angular and TOF distributions (schematic) measured at $m/z = RR'A^+$ (a and d) and $m/z = RA^+$ (b and e) for a generic $A + RR'H$ reaction giving two different indicated product channels, together with the relative velocity vector ('Newton') diagram. The circles in the Newton diagram delimit the maximum speeds of the two different products, RR′A and RA, and the corresponding ranges of their LAB scattering angles; for the RA product the LAB and CM velocities, v_{RA} and u_{RA}, and angles, Θ and θ, respectively, are also indicated. In all panels dashed and dotted lines indicate the RR′A and RA products, respectively; in panel (b) the continuous line indicates the total angular distribution recorded at $m/z = RA^+$, corresponding to the sum of the two contributions, one due to RA and the other due to the RR′A dissociative ionisation (this is the typical result when using hard ionisation detection). In panel (c) and (f) the dotted line indicates the angular and TOF distributions, respectively, of the RA product as can be obtained by using soft ionisation, i.e. an electron energy for detection lower than the appearance energy of RA^+ from RR′A via dissociative ionisation.

$RR'A^+$ one can measure the angular (figure 2a) and velocity (figure 2d) distributions of the RR′A product. In contrast, by setting the mass spectrometer at $m/z = RA^+$, if the product RR′A generates also RA^+ by dissociative ionisation, one will measure the angular and velocity distributions of both RR′A and RA products (see figures 2b and 2e, respectively); in this case, high-resolution angular and TOF distribution measurements can permit to disentangle the two contributions on the basis of the different velocity distributions and angular scattering ranges (see the Newton diagram in figure 2, and figures 2b and 2e). Remarkably, if the appearance energy (AE) of RA^+ from RR′A is sufficiently higher than the ionisation energy (IE) of RA, one can tune the electron energy below the AE threshold and detect RA free from interferences by the fragments of the heavier RR′A product. In this case the angular distribution and TOF spectra at $m/z = RA^+$ will exhibit only the features of the RA product (see figures 2c and 2f, and section 4 for practical examples). In these cases a weighted total CM differential cross-section reflecting the various possible contributions is used in the data analysis of the LAB distributions for a specific m/z, that is:

$$I_{CM}(\theta, E_T') = \sum_i w_i \times [T(\theta) \times P(E_T')]_i$$

with the parameter w_i representing the relative contribution of the integral cross-section of the ith channel.

2.3. *Crossed molecular beam experiments with variable beam crossing angle*

The relative collision energy in a CMB experiment is given by $E_c = 1/2\,\mu v_r^2$, where μ is the reduced mass of the system and v_r is the relative velocity. In general:

$$v_r^2 = v_1^2 + v_2^2 - 2v_1 v_2 \cos\gamma$$

where v_1 and v_2 are the two reactant beam velocities in the LAB frame and γ the crossing angle of the two beams (see figure 3) [19, 20, 67, 69]. Traditionally, CMB instruments with rotatable mass spectrometer detector have always featured a beam crossing angle of 90° (see, for instance, figure 1 and figure 3 (middle panel)); in this case $v_r^2 = v_1^2 + v_2^2$. The main difference between the various existing CMB instruments lies in whether the beam sources are fixed and the detector rotating, or vice versa. The fixed-detector configuration is usually adopted when photo-ionisation (by VUV laser [90] or synchrotron radiation [10, 78–80]) is employed for product detection.

In many practical cases it is of interest to study the reaction dynamics of a system as a function of collision energy. In order to change the collision energy one needs to change v_r and this, in apparatuses with $\gamma = 90°$, is achieved by changing the velocity of one or both beams. In most cases, the increase of the beam velocities leads to a reduction in angular and velocity resolution, because v_{CM} increases as well and consequently the Newton circle within which the product is confined to be scattered moves away from the LAB velocity origin. This causes (i) the product velocities to become larger in the LAB frame, to which correspond TOF spectra peaked at small values of time and distributed over a small number of channels, and (ii) the product angular distribution to distribute over a narrow LAB angular range. Also, when changing the beam conditions to vary their velocity (for example, by varying the nozzle temperature and/or the seeding gas), it is more difficult to follow the trend of the

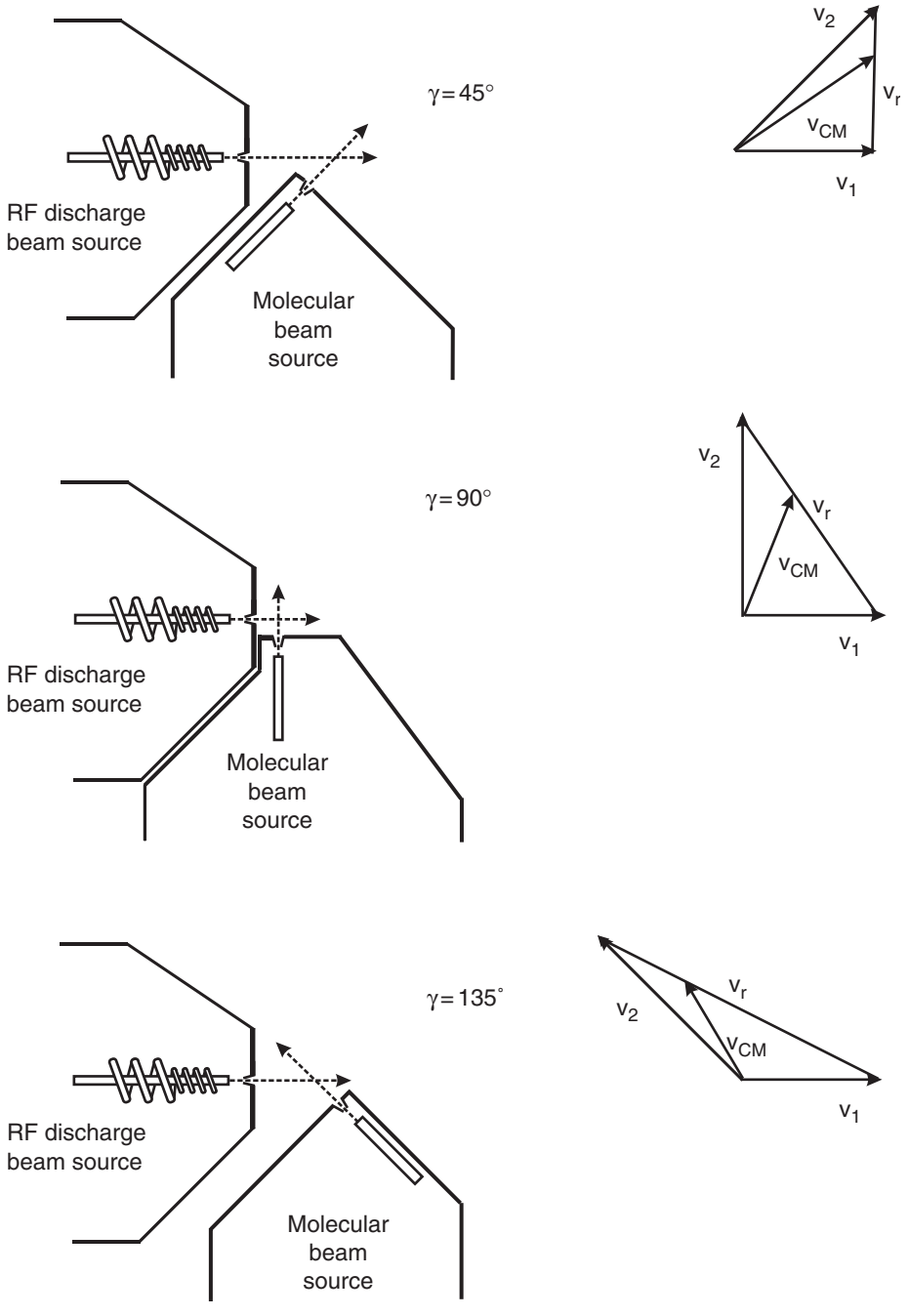

Figure 3. CMB set-ups (schematic) with beam intersection angle γ of 45° (top), 90° (middle), and 135° (bottom), and corresponding qualitative Newton diagrams with beam velocities, relative velocity, v_r, and velocity of the centre-of-mass, v_{CM}, indicated for a generic collision between two particles of mass m_1 and m_2, with $m_2 > m_1$. Given the same beam velocities in all three cases, note the increase in v_r and the reduction of v_{CM} when going from $\gamma = 45°$ to $\gamma = 135°$.

cross-sections as a function of E_c. In this respect it is much more convenient to vary the collision energy while keeping the same beam characteristics (i.e. internal temperature and speed ratio); this can be achieved by varying the intersection angle of the two beams [see refs. 19, 20 and 67].

Very recently, in our CMB apparatus we have implemented a variable beam crossing set-up with the two reactant beams crossing at $\gamma = 45^\circ$, or 90°, or 135° (see figure 3) [12]. These new settings allow us to vary the collision energy in a much wider range than previously possible. In addition, by using the $\gamma = 135^\circ$ geometry we can increase the collision energy and, at the same time, increase both angular and velocity resolution. In this case, in fact, the Newton circle within which the products are energetically confined becomes closer to the LAB velocity origin than in the $\gamma = 90^\circ$ case. With the beam velocities remaining constant, the $\gamma = 135^\circ$ configuration actually implies that the product angular distribution in the LAB frame will extend over a broader angular range and the product TOF distributions will be slower and distributed over a larger number of channels than those associated to the $\gamma = 90^\circ$ configuration. In section 4.3 we will witness the advantages obtained for the $O(^3P) + C_2H_4$ reaction when using $\gamma = 135^\circ$ instead of $\gamma = 90^\circ$.

Conversely, the $\gamma = 45^\circ$ arrangement is intended for reaching very low collision energies, because v_r decreases significantly with respect to the $\gamma = 90^\circ$ set-up, and this is of interest when studying reactions of relevance in astrochemistry, such as those of $C(^3P)$ with unsaturated hydrocarbons (see section 4.2). In this case one loses some angular and velocity resolution with respect to $\gamma = 90^\circ$, but gains some sensitivity (because the product flux is confined to a narrow angular range) and the capability of exploring strongly exoergic processes in the full angular range. For instance, by using $\gamma = 45^\circ$, 90°, and 135° configurations we have recently been able to explore the dynamics of the $C(^3P) + C_2H_2$ reaction from 3.5 kJ mol^{-1} up to more than 50 kJ mol^{-1}, and to probe the full angular range of also the strongly exoergic reaction channel $C(^1D) + C_2H_2 \rightarrow C_3 + H_2$ ($\Delta H_0^\circ = -228$ kJ mol^{-1}) (see section 4.2) [94].

2.4. *Supersonic sources of radical beams*

A prerequisite for measuring reactive DCS for the systems reviewed in this article has been the capability of generating intense, continuous supersonic beams of $O(^3P,^1D)$, $C(^3P,^1D)$, and $N(^2D)$ atoms. The technique used is quite general and is the one employed for a number of years in our laboratory. It is based on a high-pressure, high-power radio-frequency discharge beam source [8, 95], originally developed for generating $O(^3P, ^1D)$ beams [8, 96], and then adapted for producing supersonic beams of a wide variety of atomic and molecular radicals (O, N, C, Cl, OH, CN) starting from dilute mixtures (1–5%) of suitable precursor molecules (O_2, N_2, CO_2, Cl_2, H_2O, CO_2/N_2) seeded in a rare gas carrier. The detailed characteristics of the beams of the various species can be found in the relevant references.

3. Triatomic insertion reactions

It is well recognized that in reaction dynamics a strong interaction between experiment and theory is crucial. Indeed, only the direct comparison between detailed experimental

observables, such as the differential cross-section, and quantum scattering calculations can assess the quality of a computed PES and, in turn, allow the knowledge of the factors which rule a chemical transformation. Until very recently, such an ambitious goal was achieved only for a few simple reactions, i.e. $H + H_2$, $F + H_2$, and $Cl + H_2$ [7, 9, 14, 27, 32–36, 38–41, 48, 49, 97, 98]. These three benchmark systems belong to the same family of *abstraction* reactions, that is, reactions that follow a direct, rebound mechanism. In those cases, the comparison between experimental results and accurate QM scattering calculations has always led to an improvement of the calculated *ab initio* PESs, and important effects, such as those due to spin–orbit coupling [40–44, 99] or geometric phase [32–34, 100] have been examined.

The same combined experimental and theoretical approach has been extended only more recently to the case of the more complex family of *insertion* reactions, that follow an indirect mechanism and are characterised by the presence of a deep well on their PES. The best known *insertion* reactions involve electronically excited atoms and occur on multiple PESs. For instance, the reaction

$$O(^1D) + H_2(X^1\Sigma_g^+, v = 0, j) \rightarrow OH(X^2\Pi, v', j') + H(^2S) \quad \Delta H_0^\circ = -181.4\,\mathrm{kJ\,mol^{-1}} \quad (1)$$

has initially attracted a great deal of attention because of its relevance in a variety of chemical environments, and has long been regarded as the prototypical *insertion* reaction (see below). More recently, other reactive systems such as $S(^1D) + H_2 \rightarrow SH + H$ and

$$C(^1D) + H_2(X^1\Sigma_g^+, v = 0, j) \rightarrow CH(X^2\Pi, v', j') + H(^2S) \quad \Delta H_0^\circ = -25.5\,\mathrm{kJ\,mol^{-1}} \quad (2)$$

$$N(^2D) + H_2(X^1\Sigma_g^+, v = 0, j) \rightarrow NH(X^3\Sigma^-, v', j') + H(^2S) \quad \Delta H_0^\circ = -138.9\,\mathrm{kJ\,mol^{-1}} \quad (3)$$

have aroused experimental and theoretical attention and joined the list of systems for which differential cross-sections have been measured [52–58, 61–63] and accurate PESs [101–108] have become available. A common characteristic of these insertion reactions is that the deep potential well between reactants and products is associated with strongly bound species which are formed after the insertion of the excited atom into the H–H bond, that is the molecules H_2O and H_2S in their ground states and the radicals $CH_2(\tilde{a}\ ^1A')$ and $NH_2(X^2B_1)$ (see figure 4). Because of the presence of a very deep well (of the order of a few eV), accurate QM scattering calculations are quite arduous as the wave function has to be expanded on a very large number of states. Therefore, approximate methods, such as QCT or reduced dimensionality QM calculations have been mostly used together with time-dependent methods, which, however, have not produced DCSs so far. Since insertion reactions are generally believed to proceed statistically because of the stability of the intermediate complex with respect to reactants and products, a number of statistical studies are also available. In particular, an accurate statistical model (SM) [109, 110] which includes the coupled-channel capture theory of Clary and Henshaw [111] has been recently developed and applied to the study of prototype insertion reactions, including reactions (1), (2) and (3) [55, 58, 109, 110]. A similar idea was exploited in an analogous, wave-packet based statistical study of $C(^1D) + H_2/HD/D_2$ reactions [112, 113]. The SM method developed by Manolopoulos and co-workers also allows the calculations of the DCS within the random phase approximation [55, 58, 110]. The SM results have been compared with the QM results, with a different degree of agreement for the three systems and implying a different character of reaction (2) with respect to reactions (1) and (3) [110].

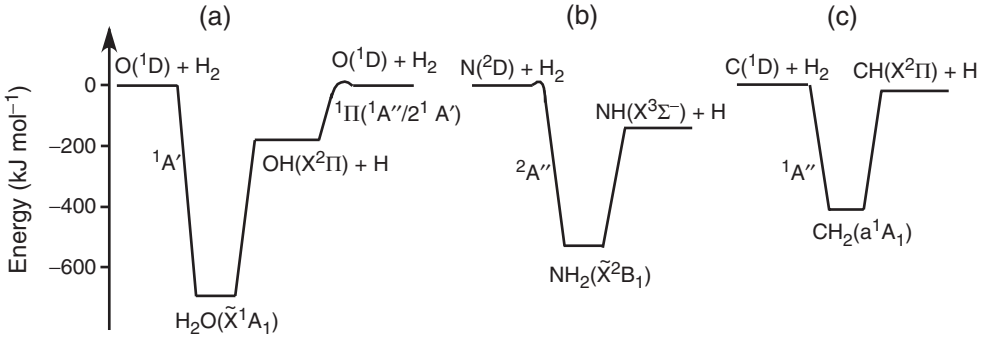

Figure 4. Energy level and correlation diagrams (schematic) for the $O(^1D) + H_2$, $N(^2D) + H_2$ and $C(^1D) + H_2$ reactions. The energy scales are the same for the three systems.

On the experimental side, these reactions are also challenging to investigate at the microscopic level, since (i) they involve electronically excited species, difficult to produce with a number density sufficient to follow a reactive study, and (ii) the radical products are formed in a multitude of rovibrational states, which makes the spectroscopic determination of their populations rather laborious – this is especially true for the very exothermic reactions (1) and (3).

In our laboratory, we have exploited the possibility of generating intense continuous beams of atomic carbon, atomic nitrogen and atomic oxygen containing a definite percentage of the atoms in their electronically excited states $C(^1D)$, $N(^2D)$ and $O(^1D)$ (see section 2.4 and Refs. 8 and 95). This has allowed us to perform CMB experiments on reactions (1), (2) and (3) [50–58, 114] almost at the same time as fully converged QM scattering calculations on accurate CH_2, NH_2 and H_2O potential energy surfaces became available for the first time [115–117]. The direct comparison of our experimental results, and those from other groups [118, 119], with the state-of-the-art QM scattering calculations by Honvault and Launay [54, 55, 57, 115, 117] allow us to assess the status reached by the theory in describing *insertion* reactions and provides us with detailed insight also on this kind of mechanism. In addition, the direct comparison between our experimental results and SM and/or QCT predictions has become a test of how realistic those approximate methods can be in the description of *insertion* reactions for which accurate PESs are available when QM calculations are not yet feasible [55, 58].

As we are going to see, each of the reactions (1), (2) and (3) has its own peculiarities. We will start by describing the $C(^1D) + H_2$ reaction, which is probably the system that best meets the expectations for insertion reactions. Then we will describe the $N(^2D) + H_2$ reaction, which is the only one, amongst those mentioned above, characterised by an activation energy. We will conclude with the $O(^1D) + H_2$ reaction, a system largely complicated by a competitive, non-insertive channel.

3.1. *Reaction $C(^1D) + H_2$*

The five-fold degenerate $C(^1D)$ atom approaching H_2 gives rise to five singlet PESs; amongst them, only two (the ground state PES, 1^1A_1, and the excited $^1B_1$) correlate with

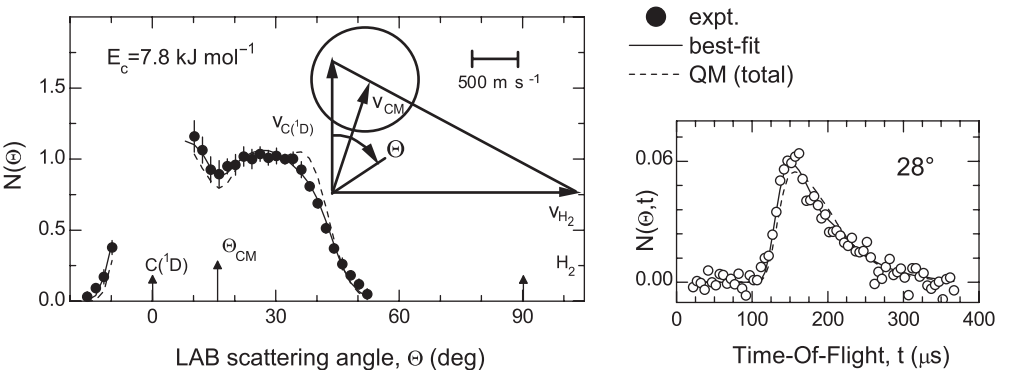

Figure 5. *Left panel*: CH product LAB angular distributions from the $C(^1D) + H_2$ reaction at $E_c = 7.8\,kJ\,mol^{-1}$ and the corresponding canonical Newton diagram. The circle in the Newton diagram delimits the maximum speed that CH can attain if all the available energy is channelled into product translation. Dots: experimental points (the error bars represent ±1 standard deviation). Solid line: best-fit angular distribution as obtained from the CM angular and translational energy distributions of figure 6. Dashed line: QM angular distribution as obtained from dynamical calculations by Honvault and Launay on the BHL PES (see text). *Right panel*: CH product time-of-flight distribution at $\Theta = 28^\circ$. Solid line and dashed lines as before. (Adapted from Ref. 57.)

the ground state products $CH(X^2\Pi) + H(^2S)$. According to the recent *ab initio* calculations by Bussery-Honvault, Honvault and Launay (BHL) [105], the first singlet $\tilde{a}\ ^1A'$ (1^1A_1) state of the CH_2 PES is characterised by a well depth of $417.1\,kJ\,mol^{-1}$ relatively to the $C(^1D) + H_2$ asymptote (see figure 4). The $\tilde{a}\ ^1A'$ surface has no barrier for the perpendicular C_{2v} geometry, but presents a large barrier of $\sim 52\,kJ\,mol^{-1}$ for the collinear $C_{\infty v}$ geometry, which prevents a contribution from a direct abstraction mechanism at low E_c's. The exit channel has no barrier for bent configurations. A peculiarity of the $\tilde{a}\ ^1A'$ CH_2 PES is the presence of two crossings with the triplet PES describing the $C(^3P) + H_2$ system, which is also characterised by the presence of a deep well corresponding to the ground state X^3B_1 of the CH_2 radical.

We have investigated reaction (2) at two different E_c of 7.8 and $16.0\,kJ\,mol^{-1}$ [56, 57] and its isotopic variant $C(^1D) + D_2(X^1\Sigma_g^+,\ v = 0, j) \rightarrow CD(X^2\Pi, v', j') + D(^2S)$ at $E_c = 15.5\,kJ\,mol^{-1}$ [58]. The LAB product angular distribution from the $C(^1D) + H_2$ reaction at $E_c = 7.8\,kJ\,mol^{-1}$ is shown in figure 5 together with the corresponding canonical Newton diagram. The error bars are also indicated representing ±1 standard deviation. The TOF distributions were recorded at nine selected laboratory angles [56, 57]; in figure 5 the TOF distribution recorded at $\Theta = 28^\circ$ is shown. The solid lines in figure 5 represent the curves calculated by using the best-fit CM functions of figure 6 [56, 57]. At this E_c, as well as at the higher E_c of $16.0\,kJ\,mol^{-1}$ and for the case of the D_2 reaction, the LAB angular distribution extends on both sides of the CM angle, Θ_{CM}. Also, the distribution is very broad, extending to the limit of energy conservation (see the related Newton diagram) and this suggests that a large fraction of the total available energy is channelled into product translation. Statistical calculations based on phase-space theory [56] were the first to indicate a strong coupling between the differential cross-section and the product translational energy distribution, $P(E_T')$, for this system. Therefore, we accounted for the coupling in the best-fit iterative procedure and found

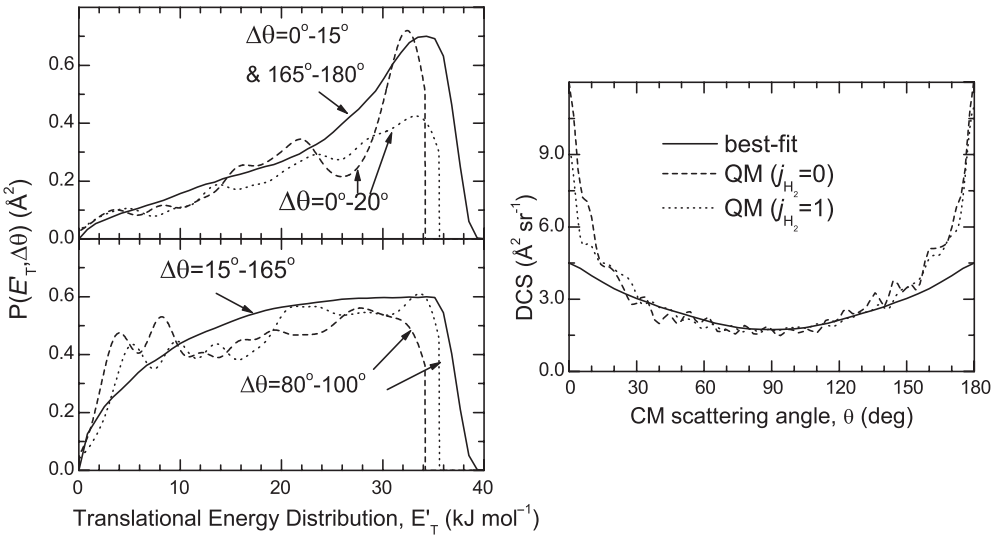

Figure 6. *Left panels*: CM scattering-angle-selected product translational energy distributions. *Right Panel*: CM product angular distributions (differential cross-sections). Solid lines: best-fit functions. Dashed lines: QM functions for H_2 in $j=0$. Dotted lines: QM functions for H_2 in $j=1$. The experimental DCS (relative units) has been arbitrarily normalized to the QM results. (Adapted from Ref. 57.)

confirmation that the angular and translational energy distributions are coupled, with a more significant fraction of energy released as product translation for the products scattered at $\theta = 0°$–$15°$ and $\theta = 165°$–$180°$. In the left panels of figure 6 the best-fit $P(E_T')$s obtained for the angular ranges $\theta = [0°$–$15°,\ 165°$–$180°]$ and $\theta = [15°$–$165°]$ are reported. The average product translational energy, defined as $\langle E_T' \rangle = \Sigma P(E_T') E_T' / \Sigma P(E_T')$, is $\sim 26\,\mathrm{kJ\,mol^{-1}}$ at the poles and $\sim 21\,\mathrm{kJ\,mol^{-1}}$ in the remaining angular range. These quantities correspond to ~73% and ~59% of the total available energy (for this experiment, the total available energy is given by $E_{tot} = E_c - \Delta H: + E_i$, where the internal energy of the reactants, E_i, was equal to the energy content of $j = 1$, which is by far the most populated level of H_2 in our beam). The best-fit CM $T(\theta)$ is backward–forward symmetric and significantly polarised (the ratio $T(90°)/T(0°, 180°)$ is 0.4 ± 0.1). Remarkably, even though the symmetry of $T(\theta)$ is not sufficient to conclude that the $C(^1D) + H_2$ reaction proceeds via a long-lived complex because of the equal probability of breaking the C–H bonds in the CH_2 intermediate, its shape is fully consistent with the insertion mechanism of $C(^1D)$ into the H–H bond.

In a recent paper [57], we have reported the comparison between our experimental results at this E_c and the accurate QM calculations performed on the BHL PES by Launay and co-workers. In figure 6 it is also shown the QM $P(E_T', \Delta\theta)$s for $\Delta\theta = 0°$–$20°$ and $\Delta\theta = 80°$–$100°$. The contributions originated by the two lowest initial rotational states of H_2 ($j = 0$ and 1) are plotted separately. We remind the reader that H_2 rotational levels up to 3 are populated in the beam, with an estimated population of 0.195; 0.708; 0.068; 0.028 for $j = 0$, 1, 2, 3, respectively [57, 116]. The experimental trend is fully confirmed by QM calculations: the fraction of energy released as product

translational energy is higher in the proximity of the two poles. However, the QM calculations systematically find fractions of energy released as product translational energy slightly smaller than the experimental ones. The QM differential cross-sections calculated at the $E_c = 7.8\,\mathrm{kJ\,mol^{-1}}$ and for the relevant initial H_2 j levels are shown in figure 6. As visible, both the best-fit and QM CM angular distributions are backward–forward symmetric, but the QM DCSs are much more polarised than the best-fit one.

To compare the theoretical results with the measured angular distribution in the most straightforward way, we have also transformed the theoretical DCSs derived in the CM frame into the LAB frame, taking into account the averaging over the experimental conditions (beam velocity distributions and angular divergences, detector aperture) and the distribution of H_2 rotational levels and their relative reactivity. Also, the angle dependent translational energy distributions as they were derived from QM calculations for each initial j were used in the simulation. The result is shown in figure 5 (dashed line). As can be appreciated, the QM calculations are able to reproduce most of the LAB angular distribution. As far as the TOF spectra are concerned, the QM simulations generate TOF distributions slightly slower than the experimental ones. Overall, the agreement between experiment and QM calculations is good, thus implying that the BHL PES gives a fairly good description of the CH_2 reactive system, but some discrepancies are clearly visible at the level of both LAB angular and TOF distributions. Some speculations can be made on their origin. On one side, we should consider that we have also a small percentage of H_2 in $j = 2$ and 3 in the beam [57] and that a larger amount of E_{tot} is associated with the reactive collisions involving them. An inclusion of their contributions in the QM simulations could help to reduce the discrepancies observed in the TOF distributions. On the other side, the discrepancies visible between the simulated and experimental angular distributions mainly originate from the strong polarisation of the calculated DCSs, as demonstrated by a sensitivity test. Interestingly, the degree of polarisation seems to reduce significantly with the increase of the initial H_2 rotational level involved and therefore an inclusion of the contributions of $j = 2$ and 3 should go in the right direction.

To understand the origin of the pronounced polarisation of the theoretical DCSs it can be useful to compare the QM results with those of the SM and QCT calculations [57, 110]. For this system the agreement between statistical and QM results is excellent and that points to the statistical nature of the $C(^1D) + H_2$ reactive system within the BHL PES [110]. In particular, the sharp peaks at the two poles of the DCSs are perfectly reproduced and, since the QCT calculation failed in reproducing them, they are believed to be of quantum nature and have been tentatively ascribed to tunnelling through the reactant and product centrifugal barriers. Since the statistical method developed by Manolopoulos and co-workers is insensitive to the collision complex region [109, 110], the pronounced polarisation can only be the result of the long range region of the BHL PES. Such a strong polarisation was not confirmed by our experiments and, therefore, the BHL PES might be not accurate enough in the long range region. Other explanations are, however, possible. For instance, a contribution from the second excited electronic state, $1A''$, surface (corresponding to the 1^1B_1 electronic state of CH_2) could also account for the differences observed [121]. The $1A''$ PES, in fact, is characterised by a large barrier ($\sim 41\,\mathrm{kJ\,mol^{-1}}$) for collinear $C_{\infty v}$ geometry and a very large barrier for perpendicular C_{2v} geometry ($\sim 347\,\mathrm{kJ\,mol^{-1}}$) [121]. However, the PES

presents no barrier for the approach with a 60° geometry and, as it was shown very recently, can significantly contribute to the reaction. Remarkably, QM scattering calculations of the $J=0$ total reaction probability as a function of the collision energy have pointed out that reactive scattering is actually more efficient on the excited $1A''$ PES rather than on the ground $1A'$ PES [121]. Therefore, it will be very interesting to compare the experimental results with the predictions of the dynamical calculations including the excited state surface contribution, when they become available. In addition, the intersystem crossing with the triplet PES could play a role because a strong spin–orbit interaction has been observed spectroscopically between the triplet and singlet states of the CH_2 radical [122–125].

The investigation of the isotopic variant $C(^1D)+D_2$ substantially confirmed the conclusions reached on reaction (2) [58]. In that case, however, only a comparison with QCT and SM calculations was possible because the relatively high experimental E_c and the deuterium substitution increase the number of states so much as to make the QM calculations prohibitive. However, since the agreement between SM and QM DCSs is very good in the case of reaction (2), and especially the degree of polarisation was always correctly reproduced, we expect that the SM DCSs are a very realistic approximation of the exact QM DCSs. Also in the case of $C(^1D)+D_2$, the discrepancies visible between the SM and experimental distributions originated from the apparently too high backward–forward to sideways intensity ratio of the calculated DCSs and also from an excessive contribution of $v'=1$.

In conclusion, the BHL PES has been found to give a fairly good description of the dynamics of reaction (2). The discrepancies observed between the QM calculations and the experimental results may be ascribed either to deficiencies in the long range region of the BHL PES or to the involvement of excited state PESs, non-adiabatic effects and intersystem crossing between the triplet and singlet PESs. Finally, the good agreement between QM and SM results points to a substantial statisticity of the reaction along the BHL PES and renders the SM method a convenient alternative to the computer-time-consuming QM calculations for some applications.

3.2. *Reaction $N(^2D)+H_2$*

The five-fold orbitally degenerate $N(^2D)$ atom interacting with H_2 gives rise to five doublet PESs (neglecting spin–orbit coupling). According to the *ab initio* calculations by Pederson *et al.* [101], the insertion pathway on the ground state PES leading to the $^2B_1$ state of NH_2 is characterised by a barrier of about $7.9\,kJ\,mol^{-1}$ for the favourite perpendicular approach. The first two excited PESs $^2A_1$ and $^2B_2$ do not correlate with ground state products, but with NH in the excited states $a^1\Delta$ and $b^1\Sigma^+$, respectively. For the collinear approach the first excited PES $^2\Delta$ has a very large barrier and the $^2\Pi$ PES is strongly repulsive. Thus, only insertion can play a role in $N(^2D)+H_2$ at the collision energies normally achieved in laboratory experiments.

In our laboratory we have investigated reaction (3) at $E_c=15.9\,kJ\,mol^{-1}$ [54, 55] and its isotopic variant $N(^2D)+D_2(X^1\sum_g^+, v=0,\ j)\rightarrow ND(X^3\Sigma^-,\ v',\ j')+D(^2S)$ at two E_c (15.9 and $21.3\,kJ\,mol^{-1}$) [52, 53]. The LAB product angular distribution from the $N(^2D)+H_2$ reaction at $E_c=15.9\,kJ\,mol^{-1}$ is shown in figure 7 together with the relative canonical Newton diagram. The error bars are also indicated representing

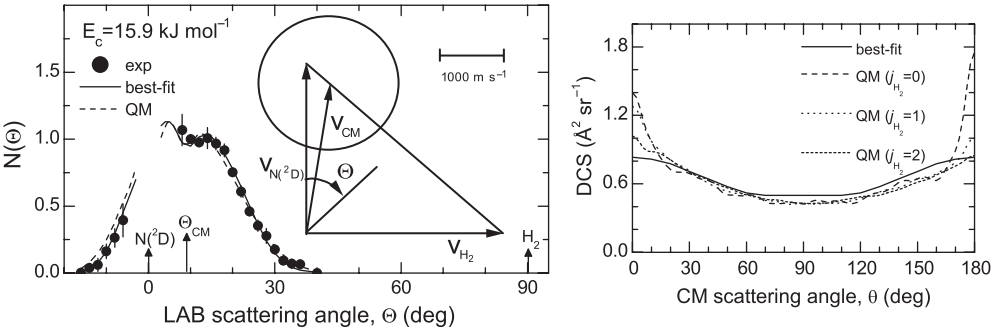

Figure 7. *Left panel*: NH product LAB angular distributions from the $N(^2D)+H_2$ reaction at $E_c = 15.9\,kJ\,mol^{-1}$ and the corresponding canonical Newton diagram. The circle in the Newton diagram delimits the maximum speed that NH can attain if all the available energy is channelled into product translation. Dots: experimental points (the error bars represent ±1 standard deviation); solid line: angular distribution as obtained from the best-fit CM angular and translational energy distributions; dashed line: QM angular distribution as obtained from dynamical calculations by Honvault and Launay on the PES by Pederson *et al.* (see text). *Right panel*: CM product angular distributions (differential cross-sections). Solid lines: best-fit functions. Dashed lines: QM DCS for H_2 in $j=0$. Dotted lines: QM DCS for H_2 in $j=1$. Short-dashed lines: QM DCS for H_2 in $j=2$. The experimental DCS (relative units) has been arbitrarily normalized to the QM results. (Adapted from Ref. 55.)

±1 standard deviation. Time-of-flight distributions (not shown here) were also recorded at four different laboratory angles. Also in this case, the angular distribution extends on both sides of Θ_{CM}, thus confirming that reaction (3) proceeds via an insertive pathway. The solid lines in figure 7 represent the curves calculated by using the best-fit CM functions reported in Ref. 55. The best-fit DCS is also shown in figure 7.

This system was the first insertion reaction for which it was possible to perform a direct comparison between the QM predictions and experimental results [54]. The QM DCSs calculated at $E_c = 15.9\,kJ\,mol^{-1}$ and for different initial H_2 j levels are displayed in figure 7 superimposed to the best-fit one. As is visible, the best-fit CM angular distribution (which is averaged over the H_2 j level population of the beam) is backward–forward symmetric, while the QM DCSs show an alternating behaviour with the DCS for $H_2(j=0)$ slightly favouring backward scattering ($\theta = 180°$) and the DCSs for $j=1$ and 2 favouring forward scattering ($\theta = 0°$). In all cases, the QM DCSs are more polarised than the best-fit one, but the polarisation reduces with the increase of the H_2 rotational level. Since it has been recognised that for reactions like $N(^2D)+H_2$ there could be a significant coupling between the product angular and translational energy distributions and that such a coupling could affect the simulation of the experimental results, in a recent paper QM, SM and QCT DCSs have been used in the simulation program of the experimental distributions by explicitly considering that coupling [55]. Also in this case, to remove any possible ambiguity associated with the derivation of the best-fit CM functions from the LAB data, the comparison between theoretical and experimental results has been performed by directly simulating the experimental distributions in the LAB frame. The angle dependent translational energy distributions, $P(E'_T, \Delta\theta)$, derived in the calculations for each initial j have been used in the simulation. The resulting angular distribution is shown in figure 7 as a dashed line. The LAB

angular and TOF distributions obtained by considering the QM angle dependent $P(E_T', \Delta\theta)$ compare well with the experimental ones. Essentially, all the characteristics of the LAB distributions are correctly predicted. However, the comparison is slightly worse with respect to that obtained when simulating the experiment without considering the coupling, that is, by using the global QM $P(E_T')$ (see figure 1 of Ref. 54). Interestingly, QCT calculations performed on the same PES at the same E_c derived CM DCSs with some propensity for backward scattering, that is in the opposite direction with respect to the QM calculations [54, 55]. The comparison between QCT and experimental angular distribution was, therefore, less satisfactory than for QM calculations [54, 55]. As far as the SM simulation is concerned, the resulting LAB distributions have been rather disappointing since at the level of the CM DCSs it is the method which better reproduces the best-fit (symmetric) CM angular distribution [55]. However, the reason for such a disagreement in the LAB frame is mostly due to the significantly large fraction of energy released as product translational energy associated with the range of θ around 90° predicted by the SM calculations.

To understand the origin of the differences between the classical and quantum predictions, in Refs. 54 and 55 the QM, QCT and SM $(2L+1)$-degeneracy-weighted reaction probabilities as a function of the orbital angular momentum L have been analysed and the DCSs scrutinised as they change with the maximum value of the angular momentum, L_{max}, retained in the partial wave sum. Interestingly, the QCT reactivity at large L is smaller than the QM one, while there is an excellent agreement between the QM and SM functions. If the reaction under study were a direct reaction, being in that case the forward scattering associated with large angular momenta (or, in classical mechanics, with large impact parameters) the smaller reactivity of larger L could directly explain the missing QCT forward scattering intensity. This was indeed the case of the *abstraction* $F + H_2$ reaction, where the largest difference between classical and quantum angular distributions was seen to occur in the forward direction and was attributed to tunnelling through the centrifugal barrier [126]. In the case of reaction (3), which is an indirect reaction, all the impact parameters (and consequently all values of L) contribute to generate intensity in the whole angular range. Nevertheless, some considerations can still be made. As a matter of fact, in Refs. 54 and 55 the analysis of QM, QCT and SM DCSs as they change with the maximum value of the angular momentum retained in the partial wave sum calculations has brought to the conclusion that the missing forward intensity in the QCT DCS is due to inability of the classical approach to consider the tunnelling through the centrifugal barriers at the highest total angular momenta that contribute to the reactions. When retaining only the first partial waves, the QM and QCT DCSs are essentially coincident, while already at $L_{max} = 10$ a clear difference becomes visible with the QM DCS having a larger intensity in the forward direction than the QCT ones. The same comparison with the SM functions reveals an excellent agreement for most of the angular range and values of L_{max}. An important limitation of the SM method, however, is due to the random-phase approximation used to generate the DCSs, which can only produce backward–forward symmetric functions. Therefore, we cannot expect that the asymmetry of the QM DCSs could be reproduced in any case. In spite of that, the SM ratio of sideways to forward scattering is always in excellent agreement with the QM functions for all values of L_{max} [55].

In conclusion, the accuracy of the NH_2 ground state PES of Pederson *et al.* [101] is substantially supported by the comparison between experimental results and state-of-the-art QM calculations. In this respect it should be noted that the *ab initio* calculations showed that more than one PES may actually contribute to insertion [102], although the ground state should be dominant. The other possible pathway involves the $^2A_1$ PES which is adiabatically connected to the $^2B_2$ state via non-C_{2v} geometry (a conical intersection exists between $^2A_1$ and $^2B_2$ surfaces), and is coupled to $^2B_1$ via Renner–Teller interaction [102]. The $^2B_2$ surface has a modest barrier of only 14.2 kJ mol^{-1} for C_{2v} geometry [102]. The role of the excited state $^2A_1$ PES has been recently analysed. A trajectory-surface-hopping study [127] revealed that the non-adiabatic DCSs, which can account for maximum contribution of 10% to the overall formation of $NH(X^3\Sigma^-)$ at collision energies around 20 kJ mol^{-1}, are clearly more backward–forward symmetric than those generated on the ground state PES. Inclusion of such a contribution can therefore help to improve the comparison with the experimental results.

Another conclusion is that for this system the limits of the approximate SM and QCT methods are clearly visible. Remarkably, the rigorous statistical model can accurately describe some important quantum effects, but cannot predict the partial asymmetry of the DCSs and fails in the prediction of less averaged quantities [55]. This is not surprising as the large exothermicity of the system is expected to render it less statistical. For a system to behave statistically, in fact, the potential well should be deep with respect to both reactant and product asymptotes. As far as the QCT predictions are concerned, the impossibility to reproduce the tunnelling through the combined centrifugal and potential barrier in the entrance channel seems to affect not only the prediction of the room temperature rate constant [54], but also the shape of the DCS.

3.3. *Reaction $O(^1D) + H_2$*

Reaction (1) has been extensively studied from both experimental and theoretical points of view because of its practical and fundamental relevance (see references in Refs. 50, 51). After such a conspicuous amount of work, it is now well established that its dynamics is largely complicated by two excited state PESs through adiabatic and non-adiabatic pathways. Also in this case, in fact, the five-fold $^1D_2$ electronic state of atomic oxygen splits into five singlet potential energy surfaces (three A' and two A'' states in C_s symmetry). Amongst the five singlet PESs, the first three may contribute to the reaction under the conditions of the available experiments. The lowest $1^1A'$ adiabatic surface correlates with the ground state products, $OH(^2\Pi) + H(^2S)$, through the ground electronic state of H_2O without barriers [104, 128]. The second $2^1A'$ surface has a collinear abstraction barrier of about 9 kJ mol^{-1} and adiabatically correlates with the excited state products, $OH(a^2\Sigma^+) + H(^2S)$; however, this surface is electronically coupled to the ground $1^1A'$ PES and can contribute to the production of $OH(^2\pi) + H(^2S)$ via non-adiabatic transitions [104]. Finally, the $1^1A''$ excited state PES is characterised by a collinear abstraction barrier of about 9 kJ mol^{-1} (the $2^1A'$ and $1^1A''$ correspond to the doubly degenerate Π state in linear geometry) and adiabatically correlates with the ground state $OH(^2\Pi) + H(^2S)$ products [104, 129]. The two upper $3^1A'$ and $2^1A''$ PESs

(corresponding to the degenerate Δ state in the $C_{\infty v}$ symmetry) are repulsive and correlate with the product excited states.

The dynamics of reaction (1) and of its isotopic variants $O(^1D) + D_2/O(^1D) + HD$ has been investigated with a variety of experimental techniques [35, 36, 50, 51, 59, 60, 118, 119, 130–146]. In particular, the reactive DCS has been determined by CMB method coupled to mass spectrometric detection [50, 51, 114, 146], Doppler-selected TOF [133, 134, 144, 145], ion-imaging [136] and Rydberg tagging TOF [35, 36, 118, 130–132] techniques. The dependence of the integral cross-section on the collision energy (excitation function) has also been investigated by Liu and co-workers [59, 60]. Finally, by using the polarised Doppler-resolved LIF technique (in a room-temperature bulb, but under single collision conditions) the product-state-resolved DCSs, excitation functions, and rotational angular momentum alignments were reported for the channels leading to several rovibrational states of OH [119, 140–142].

When comparing the experimental results with the scattering calculations on the ground $1^1A'$ state PES, the only one considered in the early theoretical studies because it is barrierless, significant discrepancies were noted in many cases [35, 50, 51, 143]. This has prompted theoreticians to consider also the contribution of the first two excited states. A first attempt in this direction was made by Kuntz *et al.* [147–150], who performed a surface hopping trajectory study that included the lowest two A′ states, as obtained from a Diatomics-In-Molecules (DIM) calculation. The DIM-PES for the excited states, however, was characterised by a quite large ($\sim 15\,kJ\,mol^{-1}$) barrier, which generates a very small excited state contribution to the reactive cross-section for the energies of the experimental data available. The role of the $1^1A''$ PES was first explored by Schatz *et al.* [129] who derived, in addition to the ground state PES [128], an *ab initio* excited state $1^1A'$ PES and included it in an adiabatic fashion in their QCT calculations [129]. Since then, the effect of the excited state PESs has been explored with a variety of theoretical methods [151–156] both on the PESs developed by Schatz and co-workers [128, 129] and on the more recent multiple PES derived by Dobbyn and Knowles (DK) [104], who constructed an analytical potential surface for the $1^1A'$, $2^1A'$, and $1^1A'$ states (with the inclusion of the $1^1A'$ and $2^1A'$ electronic coupling) on the basis of large-scale *ab initio* molecular orbital calculations at the multireference configuration interaction level. The results of those calculations have been compared with the experimental data available [50, 119, 129, 140–142, 145, 151–154, 156], with different degrees of agreement.

Before considering the effects of the excited state PESs on the reaction dynamics, however, it should be noted that the ground state PESs have mostly been tested by QCT and $J = 0$ or approximate time-dependent quantum (QM) calculations. Only more recently, state-of-the-art QM scattering calculations have been performed and compared with some of the available experimental results [118, 119]. A different degree of agreement has been found: on one side, the rigorous QM calculations on the $1^1A'$ and $1^1A''$ states of the DK PESs are able to reproduce the experimental rotational populations for the OH product in $v' = 4$ [119]; on the other side, the comparison with the CMB experimental results of Yang and co-workers, with partial rovibrational state resolution, at a collision energy ($E_c = 5.4\,kJ\,mol^{-1}$) much lower than the $1^1A''$ DK PES barrier, is only qualitative [118].

Bearing in mind that the theoretical predictions on the ground state might be partially inaccurate, there are also open issues on the contributions of the excited state PESs. According to the dependence of the integral cross-section on the collision energy as it was experimentally determined by Liu and co-workers [59, 60], the competitive abstraction channel becomes active already at $E_c \geq 7.5\,\mathrm{kJ\,mol^{-1}}$. Similar conclusions were reached in another CMB study from the measurements of the DCS as a function of E_c: a clear variation in the shape of the measured DCSs indicated that a competitive abstraction mechanism is active already at $E_c = 7.9\,\mathrm{kJ\,mol^{-1}}$ [114]. The inclusion of the excited state PESs in the theoretical treatment partially improves the comparison with those observables [119, 154, 156], but the agreement is not perfect. In fact, for both available PESs [104, 129] the contribution from the excited states becomes significant only at E_c higher than the calculated barrier and can account for the experimental observables only in part [118, 119, 145, 154, 156]. Also, it is a matter of debate how such contribution varies with increasing E_c: there is some experimental evidence that the abstraction mechanism generates a more sideways DCS as E_c increases and this is not well reproduced by the calculations.

We have contributed to the study of reaction (1) by investigating it at several E_c [50, 114]. With the aim to explore the dynamics of the reactions occurring on the excited state PESs we have recently investigated the isotopic variant $O(^1D) + D_2(X\ ^1\Sigma_g^+) \rightarrow OD(X\ ^2\Pi) + D(^2S)$ at $E_c = 25.9\,\mathrm{kJ\,mol^{-1}}$ [51], that is a collision energy much higher than the calculated barrier for the abstraction pathway. Several experimental techniques [133–136] have already been applied to the study of the isotopic variant $O(^1D) + D_2$, but none have extended to such a high E_c. Our experimental results have been compared with QCT calculations on the DK multiple PESs, as the high experimental E_c and the deuterium substitution increase the number of states so much as to make the QM calculations prohibitive [51].

The OD LAB angular distribution is shown in figure 8, together with the experimental best-fit CM angular distribution. The best-fit CM DCS can be directly compared with the QCT results (also shown in figure 8). Only a partial agreement is visible, as the best-fit CM angular distribution shows some propensity for forward scattering while the QCT one shows some propensity for backward scattering. As far as the product energy release is concerned, the QCT calculations correctly reproduce the present experimental determination (see Ref. 51), although the QCT distribution is somewhat broader and the maximum is slightly shifted towards lower E_T' than the experimental determination. Interestingly, the comparison carried out between the QCT $P(E_T')$ obtained on the $1^1A'$ PES and the one experimentally deduced renders a much poorer agreement, the theoretical distribution being much broader. Also in this case we have compared the experimental and theoretical results by simulating the LAB angular and TOF distributions using the QCT CM results. The resulting LAB angular distribution is superimposed to the experimental distribution in figure 8 and the agreement is not so good. In particular the peak at large angles, corresponding to the CM backward hemisphere, is more pronounced than the experimental one. This is not surprising since the fit of the experimental data was very sensitive to the broad plateau between 160° and 180°, which is essential to reproduce the peak of the LAB angular distributions at large angles. Such a plateau is not predicted by the QCT calculations. In fact, even though the $1^1A''$ PES contribution becomes more sideways with the

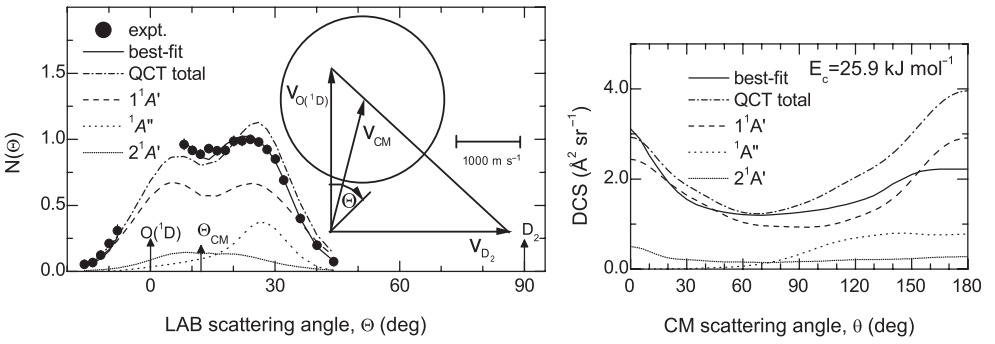

Figure 8. *Left panel*: OD product LAB angular distributions from the $O(^1D)+D_2$ reaction at $E_c = 25.9\,kJ\,mol^{-1}$ and the corresponding canonical Newton diagram. The circle in the Newton diagram delimits the maximum speed that OD can attain if all the available energy is channelled into product translation. Dots: experimental points (the error bars represent ± 1 standard deviation); solid line: angular distribution as obtained from the best-fit CM angular and translational energy distributions; dash-dot: QCT total angular distribution as obtained from the calculations by Balucani *et al.* on the PES by Dobbyn and Knowles (see text). The separate contributions, as derived from QCT calculations, from the $1^1A'$ (dash), $1^1A''$ (dot) and $2^1A'$ (short-dash) state PESs are also shown. *Right panel*: CM product angular distributions (differential cross-sections). Solid line: best-fit functions. Dash-dot: QCT total angular distribution as obtained from the calculations by Balucani *et al.* on the PES by Dobbyn and Knowles (see text). The separate contributions, as derived from QCT calculations, from the $1^1A'$ (dash), $1^1A''$ (dot) and $2^1A'$ (short-dash) state PESs are also shown. The experimental DCS (relative units) has been arbitrarily normalised to the QCT results. (Adapted from Ref. 51.)

increase of E_c, the dominant contribution of the ground $1^1A'$ PES is characterised by a backward peak. The present comparison is in line with those previously reported for the same reaction at the lower E_c of 8.4 and 13.4 kJ mol^{-1} [156] and for the other isotopic variants [35, 145].

Some speculation on the possible origin of the observed discrepancies can be done by relying on previous comparisons between accurate QM and QCT calculations for the $O(^1D)+H_2$ [118] and $N(^2D)+H_2$ reaction [54, 55]. In both cases, it has been shown that the QCT calculations on the ground $1^1A'$ PES yield DCSs with less intensity in the forward direction than the corresponding accurate QM calculations. As already commented in the previous section, the discrepancies between QCT and QM reaction probabilities and the way the QM and QCT DCSs change with the maximum value of the angular momentum retained in the partial wave sum suggest that tunnelling through the centrifugal barrier can be present also for insertion reactions [54, 55]. A similar analysis has not been performed for the reaction $O(^1D)+H_2(v=0,j=0)$ at $E_c = 5.4\,kJ\,mol^{-1}$, but in this case as well the most relevant discrepancies between the QM and QCT results occur in the angular range of the two poles ($\theta = 0^\circ$ and 180°), with the QM DCS showing a large peak in the forward direction which is not present in the QCT one [118]. Therefore, we might expect a backward bias in the QCT DCSs to be due to a classical quenching of the large impact parameters also in the case of the reaction $O(^1D)+D_2$, even though the effect of tunnelling through the centrifugal barrier is expected to be less important than in the case of the reaction with H_2.

In conclusion, the comparison between our experimental results and QCT calculations on the first three DK PESs is not satisfying. That could be due to some

deficiencies of the computed PES or to approximations associated with the QCT method. In this respect, we note that the comparison between the QM DCS and the detailed experimental results of Yang and co-workers at a collision energy below the threshold of the direct competitive channel [118] is also not satisfying. Since the direct comparison between detailed experimental observables and QM scattering calculations is the best test of the quality of a PES, the observed discrepancies between QM and the H-Rydberg tagging TOF experiment on $O(^1D) + H_2(v=0,\ j=0)$ at $E_c = 5.4\,\mathrm{kJ\,mol^{-1}}$ [118] cast some doubts on the quality of the ground state DK PES. It has been recently pointed out that the PESs [104, 128] widely used in recent calculations are not very accurate in the long-range interactions, since they neglect the intramolecular dependence of the atom–diatom dispersion coefficients and the electrostatic quadrupole–quadrupole interaction between O and H_2 [157–160]. For the reaction occurring on the ground state barrierless PES a correct treatment of the long range is certainly important, as illustrated by Manolopoulos and co-workers with their accurate approach for this and other insertion reactions [109, 110]. Also, the role of non-adiabatic effects in the product arrangement of reaction (1), where the ground state $1^1A'$ PES and the three other singlet and triplet state PESs (which correlate with the product in their ground states as well) coalesce, could influence the product distributions as recently shown [161].

4. Polyatomic multichannel reactions

After having discussed the recent progress on simple triatom insertion reactions, which are characterised by a single product channel, we move to encompass complex polyatomic reactions, which are usually characterised by several competing product channels. The determination of all product channels, their relative importance and dynamics are of central importance in the field of chemical reaction dynamics and kinetics; however, this determination has always represented a challenging task. Here, we will survey some very recent progress on this research topic achieved in our laboratory by exploiting soft EI detection and variable beam crossing angle configurations. We will see that by using the novel approach of soft EI (see section 2.1) it has become possible to tackle successfully the above challenge. We will first deal with the reactions of the simplest alkyne, acetylene (C_2H_2), with ground state oxygen, $O(^3P)$, and carbon, $C(^3P)$, atoms and will then pass, as examples of larger complexity, to those of the simplest alkene, ethylene (C_2H_4), with the same two atomic species. These reactions are of great interest in important practical areas ranging from combustion chemistry to astrochemistry. Also, they are of fundamental relevance since these systems can be considered prototypical of the category of reactions occurring via an *addition–elimination* mechanism. In these cases it is not possible to compare the experimental results with accurate theoretical predictions yet. Nevertheless, electronic structure calculations of important features (minima, transition states, product energetics) of the relevant PESs and RRKM (statistical) calculations of branching ratios can contribute substantially to characterising them. Approximate dynamical calculations, via 'direct dynamics' methods have just started to become feasible for

polyatomic reactions, but applications to the reactive systems examined here are not yet available.

4.1. *Reaction $O(^3P) + C_2H_2$*

The reaction $O(^3P) + C_2H_2$ has three energetically and spin-allowed competing channels:

$$O(^3P) + C_2H_2 \rightarrow [HCCHO]^{\dagger} \rightarrow$$

$$\rightarrow H + HCCO(X^2A'') \quad \Delta H_0^\circ = -81.6\,kJ\,mol^{-1} \quad (4a)$$

$$\rightarrow CH_2(^3B_1) + CO \quad \Delta H_0^\circ = -197.1\,kJ\,mol^{-1} \quad (4b)$$

$$\rightarrow H_2 + CCO(X^3\Sigma_g^-) \quad \Delta H_0^\circ = -93.7\,kJ\,mol^{-1} \quad (4c)$$

as well as two exoergic spin-forbidden pathways:

$$\rightarrow CH_2(^1A_1) + CO \quad \Delta H_0^\circ = -159.4\,kJ\,mol^{-1} \quad (4d)$$

$$\rightarrow H_2 + CCO(a^1\Delta) \quad \Delta H_0^\circ = -30.7\,kJ\,mol^{-1} \quad (4e)$$

From a fundamental point of view, comprising only five atoms, reaction (4) represents one of the simplest cases of polyatomic multichannel reaction. From a practical point of view, it plays a key role in the combustion of acetylene itself and also in the overall mechanism for hydrocarbon combustion [162]. Because of that, reaction (4) has been studied very extensively from the kinetic standpoint using a variety of experimental techniques [163]. While its overall rate constant has been well established ($k_{298} \sim 1.3 \times 10^{-13}$ cm^3 molecule^{-1} s^{-1}) [163], the identity of the primary reaction products and their relative importance have been a subject of considerable controversy over the years [76, 164]. The most recent, accurate kinetic determinations at room temperature have given $k(4a)/[k(4a)+k(4b)] = 0.83 \pm 0.08$ [165, 166] and $k(4b)/[k(4a)+k(4b)] = 0.17 \pm 0.08$ [166] in good agreement with theoretical predictions based on *ab initio* calculations of the triplet PES and RRKM computations [167]. Both experiment and theory indicate that the branching ratio is essentially temperature independent [165–168]. Recently, Yarkony [169] examined theoretically the possibility of non-adiabatic effects, leading to formation of $CH_2(^1A_1) + CO$, a channel (4d) which is only slightly less exoergic than that forming ground state methylene, $CH_2(^3B_1)$ (channel 4b).

CMB studies on reaction (4) became feasible in the early 1980s following the development of intense supersonic beam sources of $O(^3P)$ atoms. Two early CMB studies [164, 170] carried out in two different laboratories at a collision energy of $\sim$25 kJ mol^{-1} did not fully agree on their conclusions about the dynamics of channel (4a). An estimate of the branching ratio of channels (4a) and (4b) was carried out in one of those previous CMB studies by Schmoltner *et al.* [164] who used a beam of ^{18}O in order to be able to detect, in addition to HCCO, also ^{18}CO. A branching ratio of cross-sections $\sigma(4a)/[\sigma(4a)+\sigma(4b)] = 0.58 \pm 0.21$ was derived, which is somewhat lower than the value obtained from kinetic studies (see above).

The dynamics and branching ratios of reaction (4) under CMB conditions have been recently re-investigated in our laboratory [76] by exploiting (i) our increased instrumental sensitivity, (ii) the improved resolution for measuring product angular and TOF distributions, and (iii) the new ability to detect cleanly the CH_2 radical by using soft EI. The results, which have deepened significantly our understanding of this important combustion reaction, are summarised below.

4.1.1. Product angular and TOF distributions. In the study of the $O(^3P) + C_2H_2$ reaction using the CMB technique, while it is easy to detect the heavy HCCO (ketenyl) fragment corresponding to the H-elimination channel, the detection of any of the two co-products from the $CH_2 + CO$ channel is problematic. In particular, detection of CO is plagued by the high inherent detector background at $m/z = 28$ due to residual CO in any UHV chamber. To overcome this difficulty, Lee and co-workers [164] used a beam of isotopically labelled ^{18}O in order to detect the CO product as $C^{18}O^+$ at $m/z = 30$, which is a much cleaner mass than $m/z = 28$. Still, this could not avoid the fact that also dissociative ionisation of $HCC^{18}O$ contributes to the reactive scattering signal at $m/z = 30$. Because of that, it was not possible to measure directly the CO product angular distribution by modulating one of the two beams for background subtraction, which is the usual procedure when using continuous beams. This led to considerable uncertainty in the estimate of the branching ratio between channel (4a) and (4b) (see above).

Detection of the CH_2 counter-product at $m/z = 14$ is also problematic when employing hard EI, because of the high inherent background at this mass due to dissociative ionisation of residual CH_4 to CH_2^+ and N_2 to N^+, and of the interference from the dissociative ionisation to $^{13}CH^+$ of the main HCCO product and of the elastically scattered, intense C_2H_2 beam. Although ^{13}C represents only a very small fraction of the total C in HCCO and C_2H_2, the $^{13}CH^+$ signal from the above processes is comparable to the CH_2 reactive scattering signal when using 60 eV electrons (see figure 9b). For all these reasons, detection of CH_2 from reaction (4b) had never been attempted in the past. This, however, became recently possible in our laboratory by using the improved CMB instrument described in section 2 [12, 76]. Indeed, by using 17 eV electron energy we were able to detect CH_2 cleanly from any interference (see figure 9c), and this permitted us to measure the angular distribution of the CH_2 product by modulating the acetylene beam at 160 Hz for background subtraction. Figure 10 shows the angular distributions of the HCCO and CH_2 products at $E_c = 39.7\,kJ\,mol^{-1}$, obtained by crossing the reactant beams at $\gamma = 90^\circ$. Experiments were also performed with $\gamma = 135^\circ$; in this case, $E_c = 52.7\,kJ\,mol^{-1}$ [171]. TOF spectra were measured at numerous LAB angles for HCCO and CH_2.

Notably, the $N(\Theta)$ and $N(\Theta, t)$ at $m/z = 41$ ($HCCO^+$) and 40 (CCO^+) were found to be identical, indicating that the signal at $m/z = 40$ was all coming from the dissociative ionisation of HCCO, and not from the dynamically and energetically different H_2 elimination channels (4c) and (4e). This suggests that the H_2 elimination pathway is closed at this E_c, probably because it is characterised by a very high exit potential barrier.

From LAB product angular and TOF distributions at $m/z = 41$ and 14, CM product angular and translational energy distributions were derived for both channels (4a) and (4b) with relatively small uncertainties, especially for the HCCO channel [76].

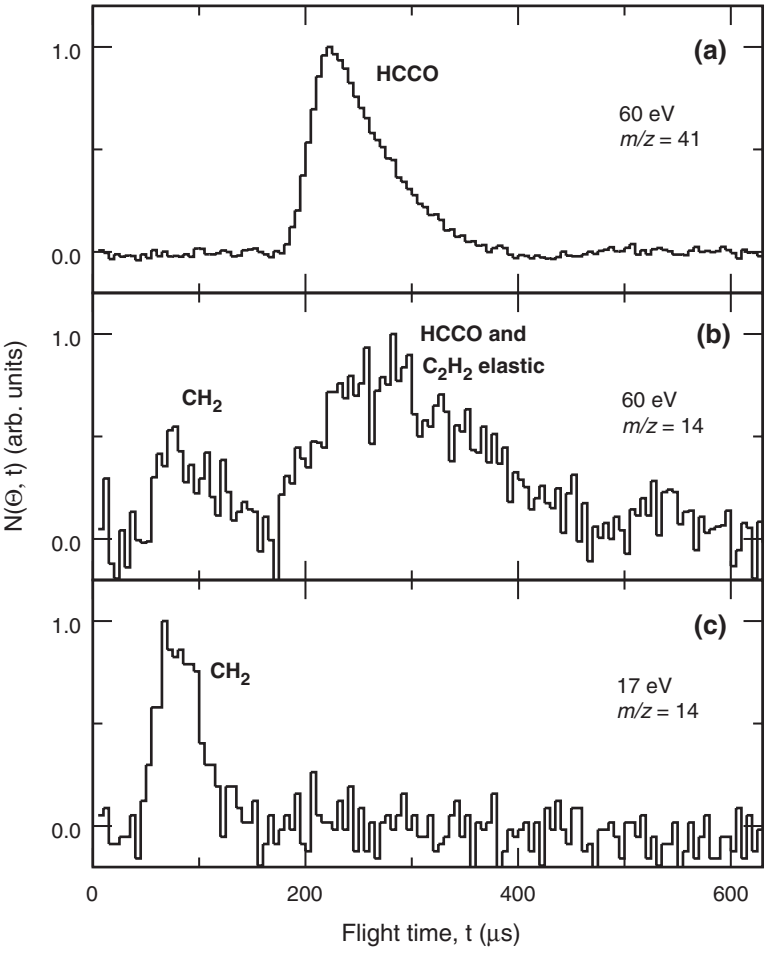

Figure 9. TOF spectra (5 μs/channel) at the LAB angle of 30° for the reaction $O(^3P) + C_2H_2$ ($E_C = 39.7\,kJ\,mol^{-1}$) at $m/z = 41$ (HCCO product) using an electron energy of 60 eV (a), at $m/z = 14$ using an electron energy of 60 eV (b), and at $m/z = 14$ using an electron energy of 17 eV (c). Note, when moving from panel (b) to panel (c) the suppression of the dissociative ionisation to $^{13}CH^+$ ($m/z = 14$) of HCCO product and elastically scattered C_2H_2 reagent.

The HCCO CM angular distribution is almost backward–forward symmetric, with some more intensity in the forward direction, and exhibits some sideways scattering. The slight asymmetry indicates that the reaction proceeds through a long-lived complex that just starts to osculate, while the sideways scattering reflects the partitioning of the total angular momentum and geometry of the decomposing HCCHO transition state. The CH_2 CM angular distribution is forward biased and this indicates that pathway (4b) is occurring through an osculating complex [76]. The fraction of total available energy channelled into translation is 0.40 for channel (4a) and 0.42 for channel (4b), which indicates the presence of an exit potential barrier for both processes; this is corroborated by electronic structure calculations of the PES [167, 168].

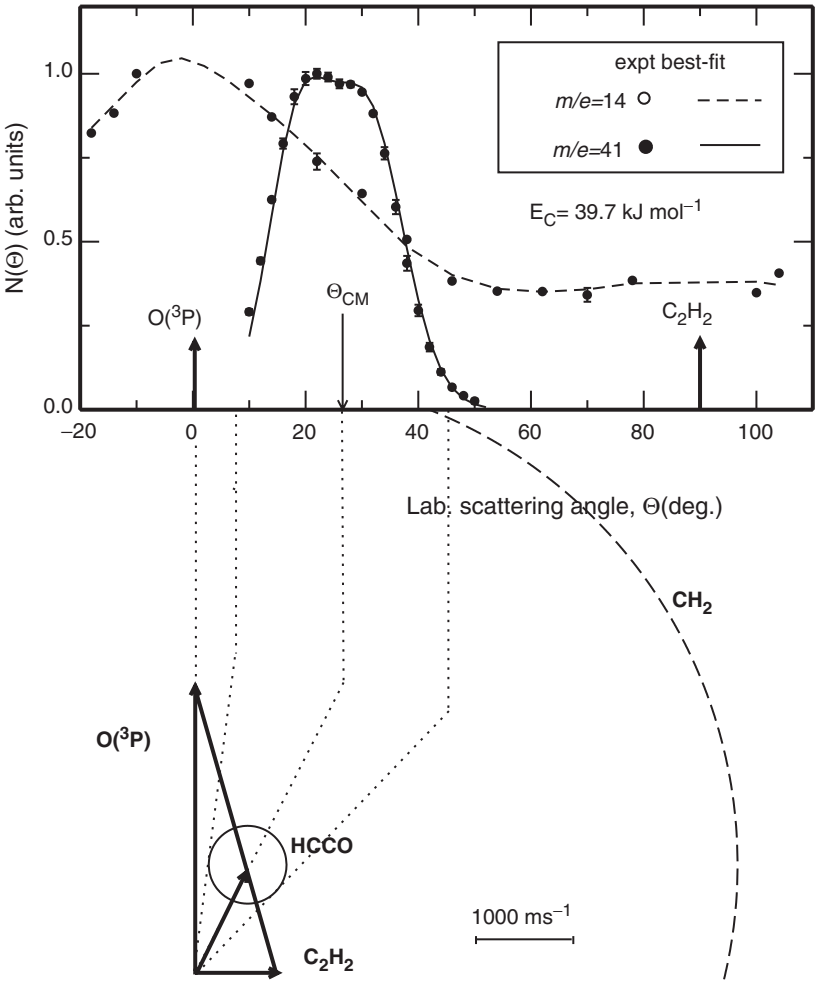

Figure 10. HCCO ($m/z = 41$) and CH_2 ($m/z = 14$) product LAB angular distributions from the $O(^3P) + C_2H_2$ reaction at $E_c = 39.7\,kJ\,mol^{-1}$. Solid and dashed lines are best-fit curves obtained from the best-fit product angular and translational energy distributions. The Newton diagram of the experiment is also shown; there the circles delimit the maximum velocity that the indicated products can attain assuming that all the available energy is channelled into translation. (Adapted from Ref. 76.)

Regarding the probability of ISC between triplet and singlet PESs leading to $CH_2(^1A_1) + CO$ formation, suggested by Yarkony [169], our results do not support the occurrence of ISC. Experimentally, because of the large exoergicity of channel (4b) and of the small energy gap ($37.6\,kJ\,mol^{-1}$) between triplet and singlet methylene it was not possible to infer from the product translational energy distribution whether singlet CH_2 was formed to any significant extent. However, the fact that the other spin-forbidden channel (4e) was also not observed indicates that ISC from the triplet to the singlet H_2CCO (ketene) PES is not occurring to an appreciable extent under our experimental conditions. Indeed, the $P(E_T')$ distribution of the $CH_2 + CO$ channel was found to peak at a very high energy value ($\sim 70\,kJ\,mol^{-1}$) [171], and this is consistent with

a dissociation process characterised by a high energy barrier in the exit channel, as in triplet-$CH_2CO \rightarrow CH_2(^3B_1) + CO$ (In contrast, it is known [172] that the process singlet-$CH_2CO \rightarrow CH_2(^1A_1) + CO$ occurs without exit potential barrier, and it would exhibit a $P(E_T')$ distribution peaking near zero).

4.1.2. Determination of branching ratios. It is of high interest for the modelling of combustion systems to know accurately the branching ratio of reaction (4). To estimate the branching ratios from CMB results one should know (i) the absolute beam intensities, (ii) the exact size of the collision volume, and (iii) the detection efficiency. These quantities are not easy to determine accurately in a CMB experiment; however, since the first two are constant and the third can be reasonably estimated, we can easily determine relative cross-sections [164]. We obtained [76, 171] the following branching ratio: $\sigma(4b)/[\sigma(4a)+\sigma(4b)] = 0.19 \pm 0.04$ that implies $\sigma(4a)/[\sigma(4a)+\sigma(4b)] = 0.81 \pm 0.0.04$. The derived values are in excellent agreement with the accurate kinetic determinations of Peeters *et al.* [165, 166] (see above) and with statistical estimates [167, 168].

In conclusion, channels (4a) and (4b) are confirmed to be the dominant channels of the reaction between $O(^3P)$ and acetylene. According to the *ab initio* calculations [168] the mechanism sees the initial electrophilic attack of the O atom to the triple bond of the C_2H_2 molecule with formation of a triplet diradical adduct (HCCHO) that, under single collision conditions can undergo competitively CH bond cleavage to HCCO + H and isomerisation to triplet ketene (H_2CCO) followed by CC bond cleavage to triplet-$CH_2 + CO$ [76, 164].

4.1.3. Determination of product ionisation energies. The novel capability of soft EI in our CMB instrument has permitted us to also measure the EI efficiency curves of the HCCO and CH_2 products as a function of electron energy, and from these to obtain, for the first time, a direct approximate estimate of the IE of the HCCO radical [171]. In fact, HCCO radicals are formed by the chemical reaction under our experimental conditions, and are therefore characterised by a certain amount of internal energy, which is about 0.5 eV according to our experimental determination. Consequently, the estimated IE may be somewhat red-shifted with respect to that of ground state HCCO.

4.2. *Reaction $C(^3P) + C_2H_2$*

The reaction of $C(^3P)$ with acetylene also exhibits chemical branching, according to three exoergic channels:

$$C(^3P) + C_2H_2(X^1\Sigma_g^+) \rightarrow [C_3H_2]^\dagger \rightarrow$$

$$\rightarrow l\text{-}C_3H(X^2\Pi_{1/2}) + H(^2S_{1/2}) \quad \Delta H_0^\circ = -1.67\,\text{kJ mol}^{-1}\ [173] \quad (5a)$$

$$\rightarrow c\text{-}C_3H(X^2B_2) + H(^2S_{1/2}) \quad \Delta H_0^\circ = -8.8\,\text{kJ mol}^{-1}\ [173] \quad (5b)$$

$$\rightarrow C_3(X^1\Sigma_g^+) + H_2(X^1\Sigma_g^+) \quad \Delta H_0^\circ = -105.9\,\text{kJ mol}^{-1} \quad (5c)$$

of which the last is spin-forbidden. With respect to the corresponding $O(^3P) + C_2H_2$ reaction, the main differences are: (i) the channel equivalent to $CH_2 + CO$ formation would be that leading to $CH_2 + C_2$, but this is strongly endoergic ($\Delta H_0^\circ = 293\,kJ\,mol^{-1}$); and (ii) the H-elimination channel now exhibits two isomeric pathways, corresponding to linear (*l*) and cyclic (*c*) C_3H formation.

Reaction (5) is known as a key process in the chemistry of the interstellar medium (ISM) and in particular of dense interstellar molecular clouds [68]. The H elimination channel synthesises the C_3H radical, observed under its cyclic and linear forms with different *c*/*l* concentration ratios in various astrophysical objects, whereas the H_2 elimination channel produces the C_3 radical which is also detected in the ISM [68]. Reaction (5) is the prototype of a host of reactions of C atoms with alkynes which are an efficient way of production of long carbon chain molecules both in the ISM and in combustion environments. Elucidating the dynamics of this reaction in a wide range of relative translational energies, including those relevant of interstellar clouds, is thus of high interest.

Kinetic studies have been performed as a function of temperature down to 15 K: the reaction has been found to be barrierless, dominated by long-range forces, and very fast ($k \sim 2$–$4 \times 10^{-10}\,cm^3\,molecule^{-1}\,s^{-1}$) down to very low temperatures [174, 175]. As such, the reaction has been included in the chemical reaction networks used to model interstellar clouds; however, until recently there was uncertainty about the nature of the reaction products and the relative branching ratios [94]. The low-temperature kinetic experiments, in fact, only measured the overall rate constant and did not detect the products. Again, for the unambiguous identification of the primary reaction products and their relative importance, CMB experiments are particularly well suited. A pioneering CMB study [176] at three E_c (8.8, 28.0, and 45.2 $kJ\,mol^{-1}$), using pulsed $C(^3P)$ beams obtained by laser ablation of graphite, identified $C_3H + H$ as the sole reaction products. A change in dynamics was observed as a function of E_c and was explained by invoking two competing microscopic channels leading to the *c*-C_3H and *l*-C_3H isomers. Formation of *c*-C_3H was suggested to occur at low E_c (and to be characterized by a forward scattered angular distribution), with contribution of *l*-C_3H taking an increasingly larger place with increasing kinetic energies (and being characterised by an isotropic angular distribution) up to become the only channel at $E_c = 45.2\,kJ\,mol^{-1}$. However, the linear and cyclic isomer contributions were not resolved in the experiment, making the conclusions about their formation dynamics and qualitative branching ratio rather tenuous.

Theoretical studies can help to elucidate the reaction mechanism, energetics and dynamics. Figure 11 depicts schematically a synthesis of the triplet and singlet C_3H_2 PES as indicated by electronic structure calculations [173, 177–179]. All recent *ab initio* calculations on the $C + C_2H_2$ reaction agree that the cyclic *c*-C_3H isomer is more stable than the linear isomer, but there exists still uncertainty on the exoergicity of process (5a) and (5b). According to a recent quantum dynamical study [180], *l*-C_3H is preferentially formed at low E_c; however, another quantum study [181] gives the opposite result, with *c*-C_3H being dominant at all collision energies.

A more recent CMB study [66–68] carried out in our laboratory at $E_c = 29.3\,kJ\,mol^{-1}$ using a continuous carbon atom beam containing both $C(^3P)$ and excited $C(^1D)$ (in a significant percentage) clearly demonstrated that, in addition to the H-elimination

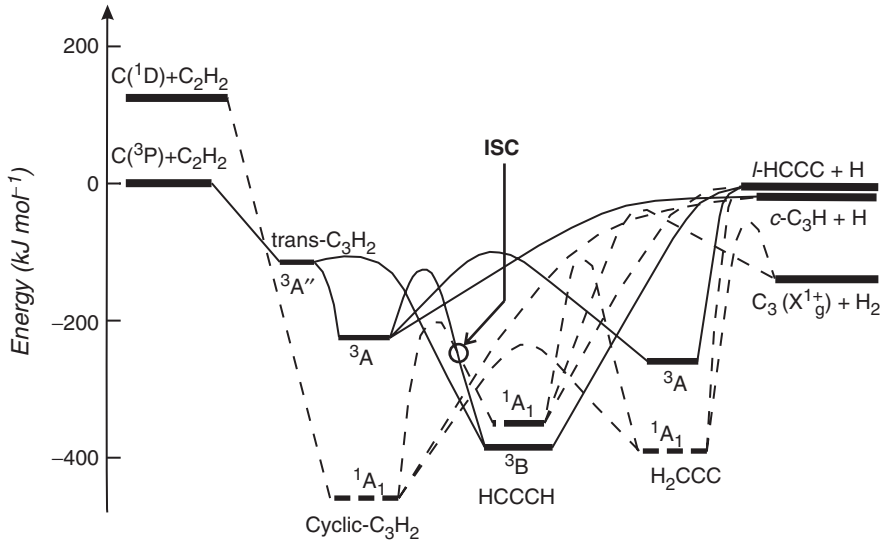

Figure 11. Schematic representation of the triplet and singlet C_3H_2 potential energy surfaces (adapted from Refs. 67, 68, and 94). The triplet–singlet seam of intersystem crossing is labelled with ISC.

channel, the strongly exoergic, spin-forbidden H_2 elimination pathway (5c) leading to $C_3(X^1\sum_g^+) + H_2(X^1\sum_g^+)$ also plays an important role through ISC between the triplet and singlet PESs (see figure 11). The branching ratio was derived to be $\sigma(C_3 + H_2)/[\sigma(C_3 + H_2) + \sigma(C_3H + H)] = 0.37$ at $E_c = 29.3\,kJ\,mol^{-1}$. This result is consistent with that of a recent experimental investigation [182] of the detailed kinetics of $C(^3P) + C_2H_2(X^1\sum_g^+)$ at 300 K, which found a branching ratio for H-production, i.e. $k_{(5a+5b)}/k_5$, of only 0.53 ± 0.04 suggesting that pathway (5c) should account for the rest (i.e. $k_{5c}/k_5 = 0.47 \pm 0.04$). *Ab initio* electronic structure calculations of the triplet and singlet PESs support this scenario by having located a triplet–singlet seam of crossing where ISC can readily occur [178] (see figure 11).

More recent experiments carried out in our laboratory with higher angular and velocity resolution at different collision energies, ranging from quite low E_c ($3.5\,kJ\,mol^{-1}$) to quite high E_c ($50\,kJ\,mol^{-1}$), achieved by crossing the two reactant beams at 45° and 135°, respectively, were able to address some unsolved questions about the dynamics of reaction (5) [94]. This study was carried out in synergistic fashion with pulsed CMB experiments in Bordeaux using VUV H-atom detection within a Doppler scheme, down to $E_c = 0.8\,kJ\,mol^{-1}$ [94].

4.2.1. H and H_2 elimination channels, and branching ratios. In our CMB experiments we have been able to investigate the dynamics of C_3H and C_3 formation from both $C(^3P)$ and $C(^1D)$. Here we limit ourselves to discuss the $C(^3P)$ dynamics. Although the C_3H products still fragment to C_3^+ even under soft EI (down to very low electron energies), the two main reaction pathways leading to H and H_2 elimination were unambiguously disentangled from differences in the $m/z = 37$ and 36 angular

distributions (see figures 12 and 13, respectively, where data at $E_c = 18.5\,kJ\,mol^{-1}$ are shown) and the observation of distinct features in the TOF measurements at $m/z = 36$ (see figure 14). In these experiments an electron ionisation energy of 25 eV was used to suppress elastic interferences from impurities in the acetylene beam. As can be seen the $m/z = 36$ angular distribution exhibits much more intensity on the wings and is wider with respect to the $m/z = 37$ angular distribution, and this indicates that signal at $m/z = 36$ is not all coming from dissociative ionisation of C_3H, but also from a dynamically different channel which corresponds to C_3 formation. Figure 14 compares four TOF spectra measured at $E_c = 18.5\,kJ\,mol^{-1}$ by detecting the product at $m/z = 37$ (only C_3H product) and $m/z = 36$ (both C_3H and C_3 products): the dominant slow peak in the $m/z = 36$ spectra corresponds to l/c-C_3H formation, while the fast, smaller peak is unambiguously attributed to C_3 formation (channel 5c), as can be inferred from the Newton diagram of the experiment (see figure 13).

CM product angular and translational energy distributions were determined at $E_c =$ 3.5 and $18.5\,kJ\,mol^{-1}$ for both l/c-$C_3H + H$ and $C_3 + H_2$ formation [94]. At the lowest E_c, formation of l/c-C_3H and C_3 from $C(^3P)$ are characterised by a backward–forward symmetric CM angular distribution which indicates that all reactions (5a–5c) proceed through the formation of a long-lived C_3H_2 complex, i.e. a complex whose lifetime is of many rotational periods. This is corroborated by statistical calculations of the lifetime of the various possible complexes on *ab initio* PESs, that found them to be of the order of tens of ps to ns at 300 K [179]. As E_c is raised to $18.5\,kJ\,mol^{-1}$, the C_3 CM angular distribution starts to be slightly forward biased, which indicates, within the osculating–complex model for chemical reactions [3, 4, 8, 67], that the lifetime of the collision complex producing it becomes comparable to its rotational period. In contrast, the CM angular distribution of l-/c-C_3H remains essentially backward–forward symmetric, indicating that the corresponding C_3H_2 complex still lives for many rotational periods. As E_c rises to $50\,kJ\,mol^{-1}$, both C_3H and C_3 angular distributions become somewhat forward peaked, indicating that the corresponding complex lifetimes become comparable to their rotational periods. A large fraction of the total available energy is channelled in product translation for all products, although there are significant differences (~40% and 60% for l-C_3H and c-C_3H, respectively, at all E_cs, while ~55% and 65% for C_3 at low and high E_c, respectively). From the extent of the $P(E_T')$ functions for linear and cyclic C_3H we were able to derive an improved exoergicity for channel (5b) [94]; the latter was found to be about $2.5\,kJ\,mol^{-1}$ larger than the theoretical value [173] of $8.6\,kJ\,mol^{-1}$.

From the experimental data we were able to estimate the branching ratios of the three possible reaction channels. The branching ratio $\sigma(C_3)/\sigma(C_3 + C_3H)$ was found to increase with decreasing E_c [94], as one may reasonably expect from the trend with E_c of the lifetime of the intermediate C_3H_2 complex: the complex lifetime increases with decreasing E_c [179], and so does the probability of ISC. In particular, at $E_c = 3.5\,kJ\,mol^{-1}$ the branching ratio was determined to be ~0.5, in good agreement with the kinetic estimate at room temperature [182] (which corresponds to an average E_c of $\sim 3.7\,kJ\,mol^{-1}$). The CMB data may be extrapolated to the low temperatures typical of cold molecular clouds, at which we predict a branching ratio of ~0.5–06. This piece of information should be included in theoretical models of cold molecular clouds.

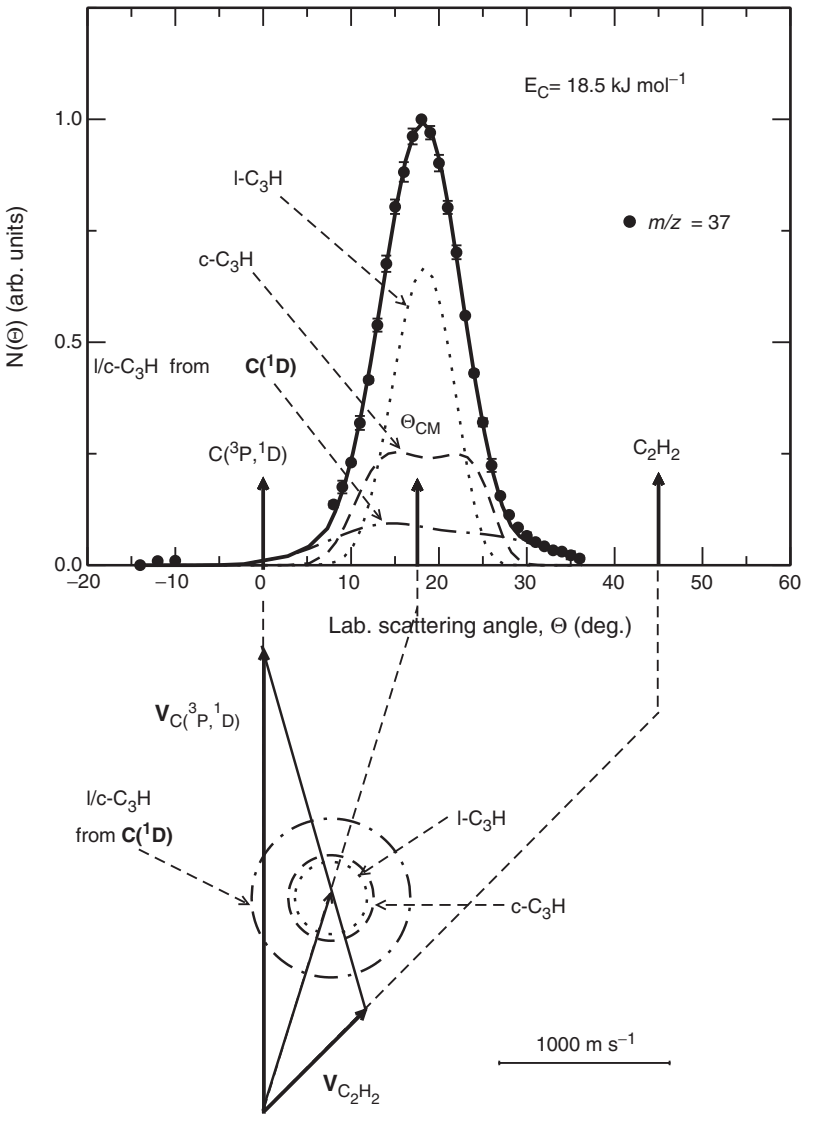

Figure 12. LAB angular distribution, N(Θ), of C_3H products at $m/z = 37$ (solid circles) from the reactions $C(^3P,^1D) + C_2H_2$ at $E_c = 18.5\,kJ\,mol^{-1}$, together with the Newton diagram of the experiment. There the circles delimit the maximum velocity that the indicated products (when from $C(^1D)$, this is labelled) can attain on the basis of linear momentum and energy conservation if all the available energy goes into product translational energy. Solid line is the total angular distribution calculated from the best-fit product CM translational energy and angular distributions for the contributing channels; the separate contributions of the two possible C_3H isomers from the $C(^3P)$ reactions are indicated with dashed (cyclic isomer) and dotted (linear isomer) line, while the contribution of *c*-/*l*-C_3H from the $C(^1D)$ reaction is indicated with dashed-dotted line. (Adapted from Ref. 94.)

Notably, at the very low E_c of $3.5\,kJ\,mol^{-1}$ it was possible to disentangle the relative contribution of the two C_3H isomeric products on the basis of their different dynamics (different CM angular and translational energy distributions) [94]. The experimental results indicate that *c*-C_3H is preferentially formed at low E_c, which is not surprising

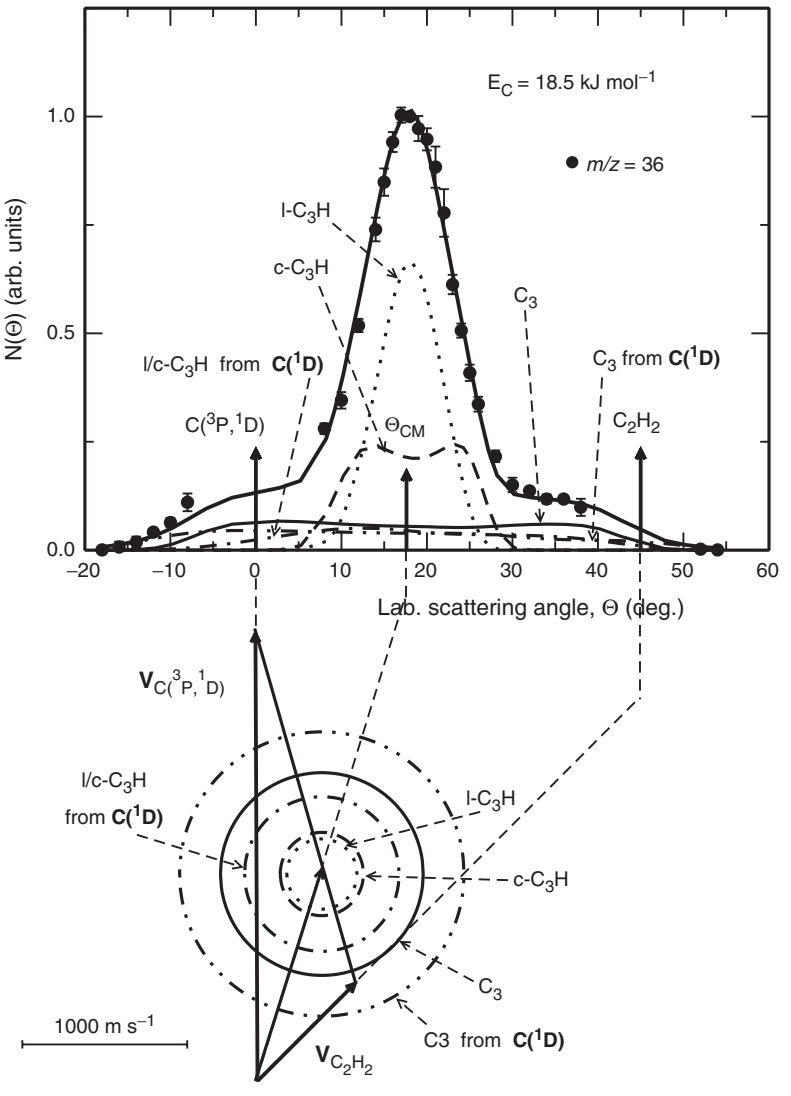

Figure 13. LAB angular distribution, N(Θ), of products at $m/z = 36$ (solid circles) from the reactions $C(^3P,^1D) + C_2H_2$ at $E_c = 18.5\,kJ\,mol^{-1}$, together with the Newton diagram of the experiment. The circles in the Newton diagram delimit the maximum velocity that the indicated products (when from $C(^1D)$, this is labelled) can attain on the basis of linear momentum and energy conservation if all the available energy goes into product translational energy. Heavy solid line is the total angular distribution calculated from the best-fit product CM translational energy and angular distributions for the contributing channels. The separate contributions of the two possible C_3H isomers and C_3 from the $C(^3P)$ reactions are indicated with dashed (cyclic C_3H isomer), dotted (linear C_3H isomer) and light solid (C_3) lines, while the contribution of *c*-/*l*-C_3H and C_3 from the $C(^1D)$ reactions are indicated with dashed-dotted line (C_3H) and dashed-double dotted (C_3) lines. (Adapted from Ref. 94.)

considering that the *l*-$C_3H + H$ pathway is very weakly exoergic. The ratio *c*-C_3H/*l*-C_3H was found to decrease with increasing E_c, from ~9 at $E_c = 0.8\,kJ\,mol^{-1}$ to ~3.4 at $E_c = 3.5\,kJ\,mol^{-1}$ and ~1.6 at $E_c = 18.5\,kJ\,mol^{-1}$ [94]. Analysis of the data at $E_c = 50.2\,kJ\,mol^{-1}$ indicates that the ratio tends to unity at higher energies [183].

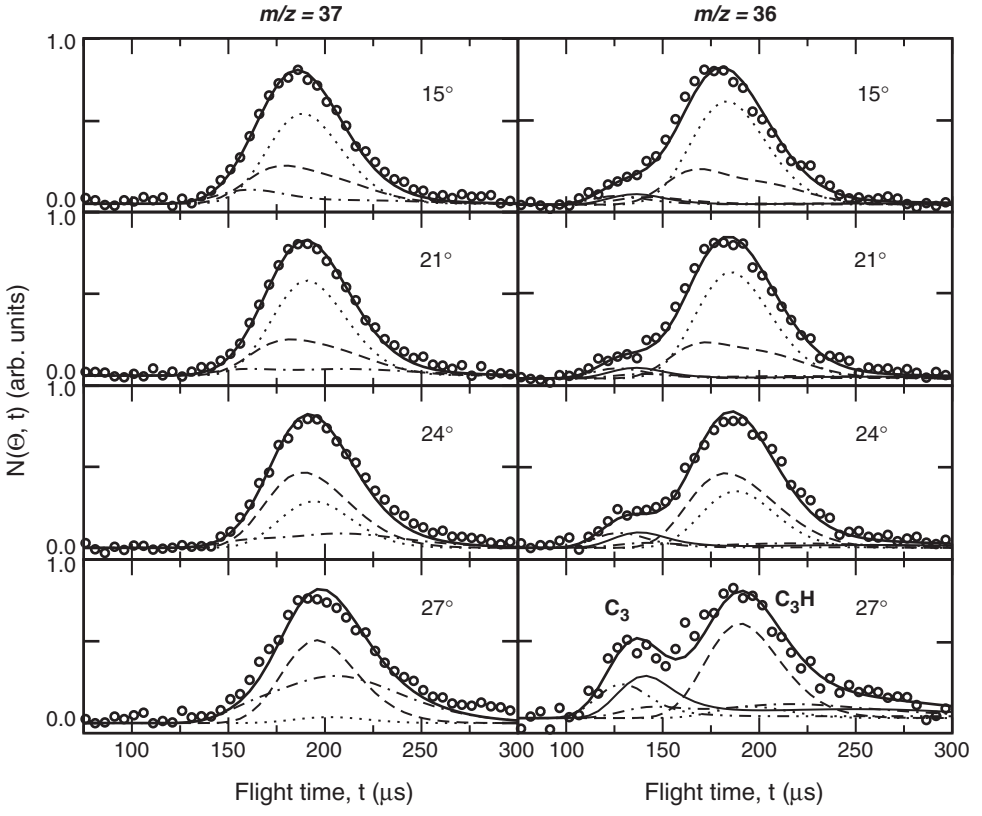

Figure 14. Exemplary TOF distributions of the $m/z = 37$ (l.h.s.) and $m/z = 36$ (r.h.s.) products (open circles) from the reactions $C(^3P,^1D) + C_2H_2$ at $E_c = 18.5\,kJ\,mol^{-1}$ at the indicated LAB angles. Symbols are as in figures 12 and 13. While the area of each spectrum at a given angle is equal to the corresponding $N(\Theta)$ intensity at that angle, here they are all normalised to 1 at the maximum for clearer display. Note the contribution of the $C_3 + H_2$ and $C_3H + H$ channels to the signal recorded at $m/z = 36$ to which the parent ion of CH_3 and the fragment ion of C_3H contribute. (Adapted from Ref. 94.)

These results contradict both quantum scattering studies in reduced dimensionality by Buonomo and Clary [180], who found *l*-C_3H preferentially formed at any energy sampled between $E_c = 5$ and $70\,kJ\,mol^{-1}$, and by Takayanagi [181], who found overwhelmingly dominant *c*-C_3H between $E_c = 0.1$ and $58\,kJ\,mol^{-1}$. Interestingly, we note that the values experimentally derived at low E_cs are close to those observed in translucent clouds [184] and in dense cloud TMC-1 [185]. More theoretical work is in order.

The dynamics of formation of the various products and their branching ratios can be rationalised with reference to the C_3H_2 PESs (figure 11). In order to understand the observed trends let us analyse the probable reaction mechanisms. According to electronic structure calculations [173, 177, 179], the first step sees the addition of the carbon atom to the acetylene molecule to form triplet cyclic-C_3H_2 which can undergo H-elimination to *c*-$C_3H + H$ or isomerise to triplet propargylene (HCCCH) or vinylidenecarbene (H_2CCC). The latter can either eliminate H to form *l*-$C_3H + H$ or

undergo ISC to singlet C_3H_2 (see figure 11). Of the three possible isomers of singlet C_3H_2, all can eliminate H, but vinylidenecarbene can also eliminate H_2 through a three-centre elimination process over a significant exit barrier (H_2-elimination on the triplet surface would lead to triplet C_3; however, this pathway is nearly thermoneutral and characterised by a very high exit potential barrier, and therefore cannot occur at the experimental collision energies). At low E_c the initially formed triplet cyclic-C_3H_2 undergoes preferential CH bond cleavage forming c-$C_3H + H$ (the most exoergic pathway). As E_c is raised, the cross-section for l-C_3H formation starts to increase with respect to that of c-C_3H, and at the highest E_c of 50.2 kJ mol^{-1}, the two C_3H isomers are formed approximately in equal amount. Because of the long lifetime of the intermediate triplet propargylene complex [179], the system has enough probability to undergo ISC from the triplet to the singlet PES [178]. The fact that the branching ratio $C_3/(C_3 + C_3H)$ decreases with increasing E_c can be traced back to the decrease of ISC probability with decreasing complex lifetime. However, a quantitative rationalisation of the detailed dynamics of each pathway and associated branching ratio as a function of E_c is a formidable task, which will require direct dynamics simulations on-the-fly on *ab initio* PESs in full dimensionality, with inclusion of non-adiabatic effects.

4.2.2. Ionisation energy of c/l-C_3H radicals. Also in this case, by measuring the EI efficiency curves as a function of electron energy for the C_3H products it was possible to obtain, for the first time, experimental information on the ionisation energy of the two C_3H isomers [183]. The estimate of ionisation energies of important radical products, difficult to produce in a clean and controlled manner otherwise, are another bonus afforded by CMB experiments using soft EI detection with tunable electron energy.

4.3. *Reaction $O(^3P) + C_2H_4$*

If we move from the acetylene to the ethylene reactions with $O(^3P)$ and $C(^3P)$, the presence of two additional hydrogen atoms (seven-atom reactions) renders the PES much more complicated and opens up a larger variety of competing pathways. For instance, the reaction of $O(^3P)$ with ethylene is more complex than that with acetylene, exhibiting six competing energetically allowed pathways:

$$O(^3P) + C_2H_4 \rightarrow [C_2H_4O]^{\dagger} \rightarrow$$

$$\rightarrow H + CH_2CHO \quad \Delta H_0^\circ = -71\ \text{kJ mol}^{-1} \tag{6a}$$

$$\rightarrow H + CH_3CO \quad \Delta H_0^\circ = -114\ \text{kJ mol}^{-1} \tag{6b}$$

$$\rightarrow H_2 + CH_2CO \quad \Delta H_0^\circ = -356\ \text{kJ mol}^{-1} \tag{6c}$$

$$\rightarrow CH_3 + HCO \quad \Delta H_0^\circ = -113\ \text{kJ mol}^{-1} \tag{6d}$$

$$\rightarrow CH_2 + HCHO \quad \Delta H_0^\circ = -29\ \text{kJ mol}^{-1} \tag{6e}$$

$$\rightarrow CH_4 + CO \quad \Delta H_0^\circ = -488\ \text{kJ mol}^{-1} \tag{6f}$$

Of these, at thermal energies channels (6c), (6d) and (6f) can only occur via ISC from the triplet to the singlet PES [186, 187].

Analogously to $O(^3P) + C_2H_2$, the $O(^3P) + C_2H_4$ reaction plays a central role, besides in the combustion of ethylene itself, in the overall mechanism for hydrocarbon combustion [162, 188]. Many research groups have investigated this reaction, employing a variety of experimental techniques under different conditions of pressure and temperature and identifying only some of the possible products [189–191]. Also in this case the overall rate constant has been well established ($k_{298} = 7.5 \times 10^{-13}\,cm^3\,molec^{-1}\,s^{-1}$) [163], but the question of the identity of the primary reaction products and their relative importance has been a subject of considerable controversy over the years.

A considerable amount of theoretical work was also carried out on this reaction [192, 193]; notably, a very comprehensive theoretical study of both triplet and singlet PESs has been published very recently by Peeters and co-workers [186], and this includes also statistical calculations of the branching ratios.

Two previous CMB studies [170, 194] at $E_c \approx 25\,kJ\,mol^{-1}$ confirmed the occurrence of channel (6a), the easiest to detect for kinematics reasons. Channels (6c, d, e) are much more difficult to detect due to unfavourable kinematics and to the fact that the expected ion signal from products of channel (6c) at $m/z = 42$, of channel (6d) at $m/z = 15$ or 29 (or 28), and of channel (6e) at $m/z = 14$ or 30, coincide with major background peaks and/or with peaks coming from dissociative ionisation of the most intense signal corresponding to CH_2CHO formation and of the elastically scattered C_2H_4 reagent.

Only the problem connected with channel (6d) was partly overcome in a previous CMB study [187] by using a beam of isotopically labelled ^{18}O, which permitted the detection of the $HC^{18}O$ product of channel (6d) at $m/z = 31$ ($HC^{18}O^+$) and 30 ($C^{18}O^+$), and to obtain an estimate of the branching ratio between channel (6a) and (6d) of 0.71 ± 0.26, a value which is somewhat larger than any previous kinetic estimate, which gave values ranging from 0.44 to 0.55 [190, 191].

4.3.1. Observation of all product channels and branching ratios. By using soft EI ionisation, in our laboratory we have been able to unambiguously detect products from the five reaction pathways (6a–e), determine their branching ratio and characterise their dynamics [77]. Here we summarise some of these results, which will exemplify the power of soft EI ionisation. From measurements of the EI efficiency curves at various m/z ratios (15, 42, and 43), it was found that the parent ion at $m/z = 43$ (CH_2CHO^+, corresponding to one of the main reaction channels, vinoxy radical formation) is not stable, so that measurements of angular and TOF distributions were carried out at $m/z = 42$. From the EI ionisation efficiency curve at $m/e = 42$ direct information on the IE of the vinoxy radical (for which no such information was previously available) was also obtained.

From a detailed series of angular and velocity distribution measurements at $m/z = 42$, 15, and 14 using different electron energies, it was possible to characterise the reaction dynamics of all five competing channels (6a–e) [77]. Figure 15 shows the LAB angular distribution recorded at $m/z = 15$ using 17 eV electron energy, with the Newton diagram of the experiment for the reaction $O(^3P) + C_2H_4$ at $E_c = 54.0\,kJ\,mol^{-1}$ (the crossing

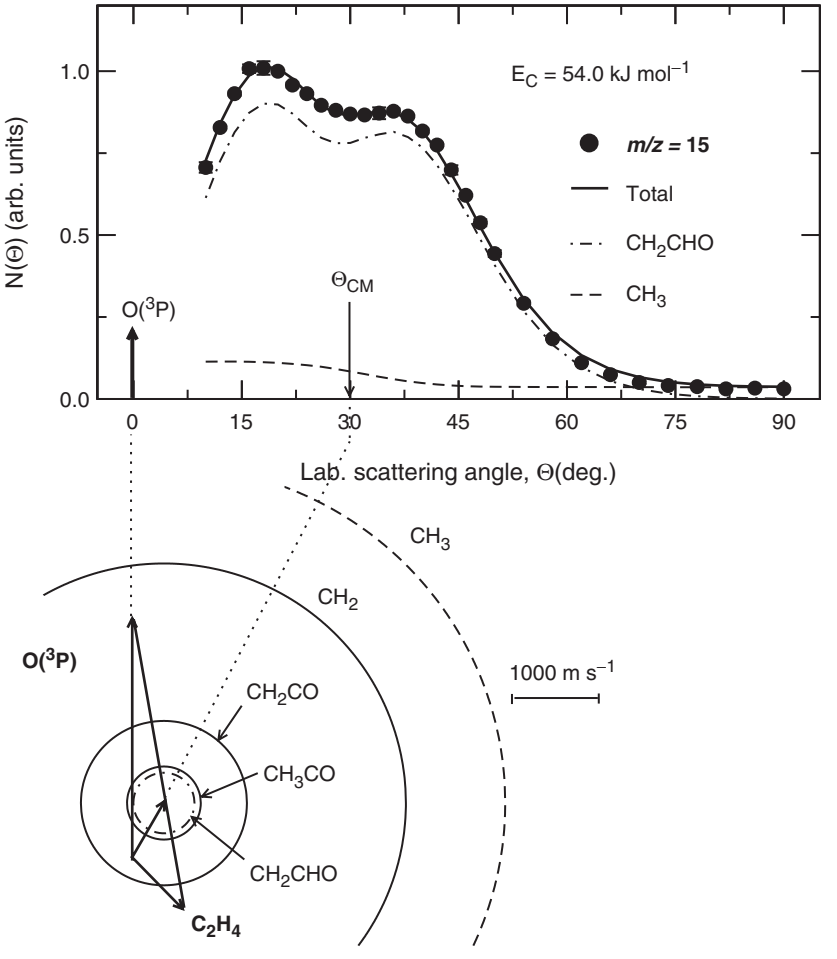

Figure 15. LAB angular distribution at $m/z = 15$ (solid circles) from the reaction $O(^3P) + C_2H_4$ at $E_c = 54.0\,kJ\,mol^{-1}$, obtained by using an electron energy of 17 eV, together with the relative Newton diagram. Error bars are indicated when visible outside the experimental dots. The circles in the Newton diagram delimit the maximum speed that the indicated products can attain on the basis of energy and linear momentum conservation if all the available energy goes into product translation. Heavy solid line is the total angular distribution calculated from the best-fit product CM translational energy and angular distributions, the separate contributions from the CH_2CHO and CH_3 products from channels (6a) and (6d) being shown with dashed-dotted and dashed line, respectively. (Adapted from Ref. 77.)

beam configuration with $\gamma = 135^\circ$ was used for higher angular and especially TOF resolution). Two channels (6a and 6d) contribute to this signal; the relative contributions are disentangled through TOF measurements at selected LAB angles (as an example, see top of figure 16, where the TOF spectrum at $\Theta = 34^\circ$ is shown). Figure 16 (bottom) shows also one of the TOF spectra recorded at $m/z = 42$ and used to disentangle the relative contributions of channel (6a), (6b), and (6c). Figure 17 (bottom) shows instead the TOF spectrum recorded at $m/z = 14$, again with an electron energy of

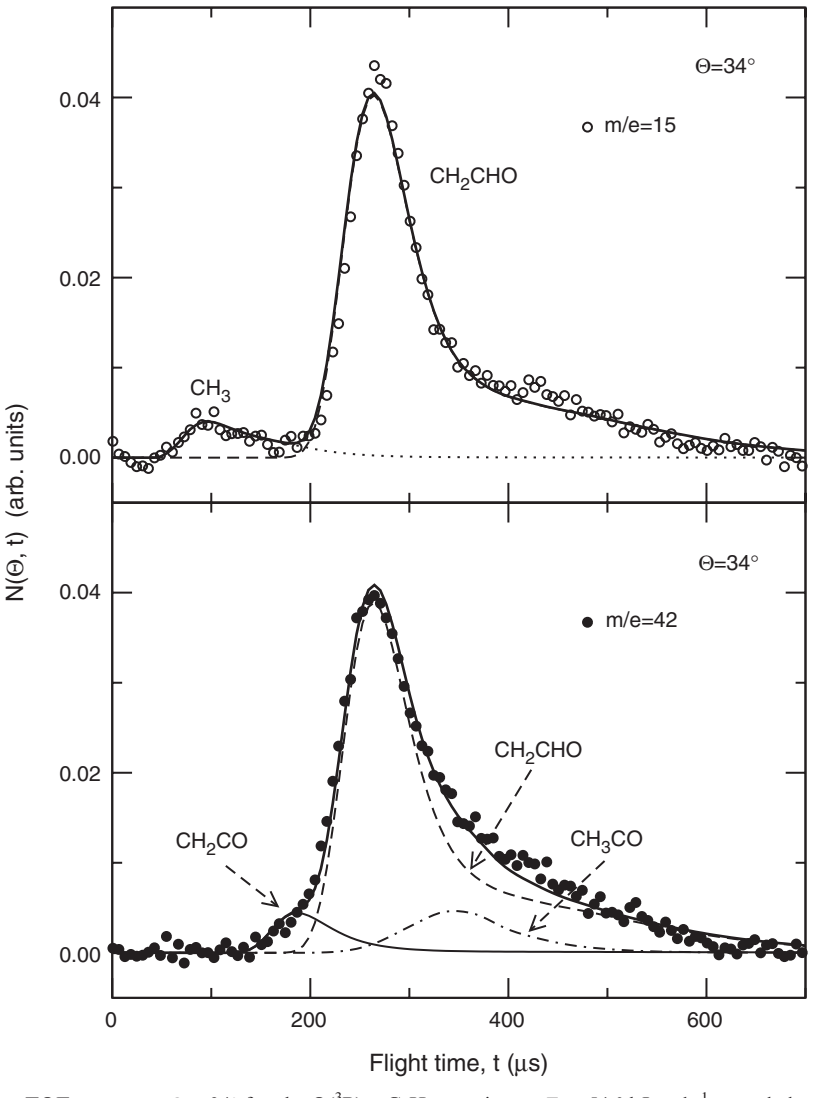

Figure 16. TOF spectra at $\Theta = 34^\circ$ for the $O(^3P) + C_2H_4$ reaction at $E_c = 54.0\,kJ\,mol^{-1}$ recorded at $m/z = 15$ (top) and 42 (bottom) using an electron energy of 17 eV. Open circles are experimental points; heavy solid lines are the total TOF distributions calculated from the best-fit product CM translational energy and angular distributions for the contributing channels. The various contributions (depicted with different lines) are marked with the formula of the corresponding product. Note that three channels contribute to products detected at $m/z = 42$ and two channels to products detected at $m/z = 15$. (Adapted from Ref. 77.)

17 eV, at the LAB angle $\Theta = 34^\circ$. As derived from the data analysis [77], and as clearly shown in the figures 16 and 17, these TOF spectra carry the fingerprints of all five possible product channels (6a–e). Specifically, the $m/z = 15$ TOF spectrum exhibits a fast peak which is unambiguously due to the CH_3 from the $CH_3 + HCO$ channel (reaction 6d), and a slower, more intense peak, due to dissociative ionisation in the

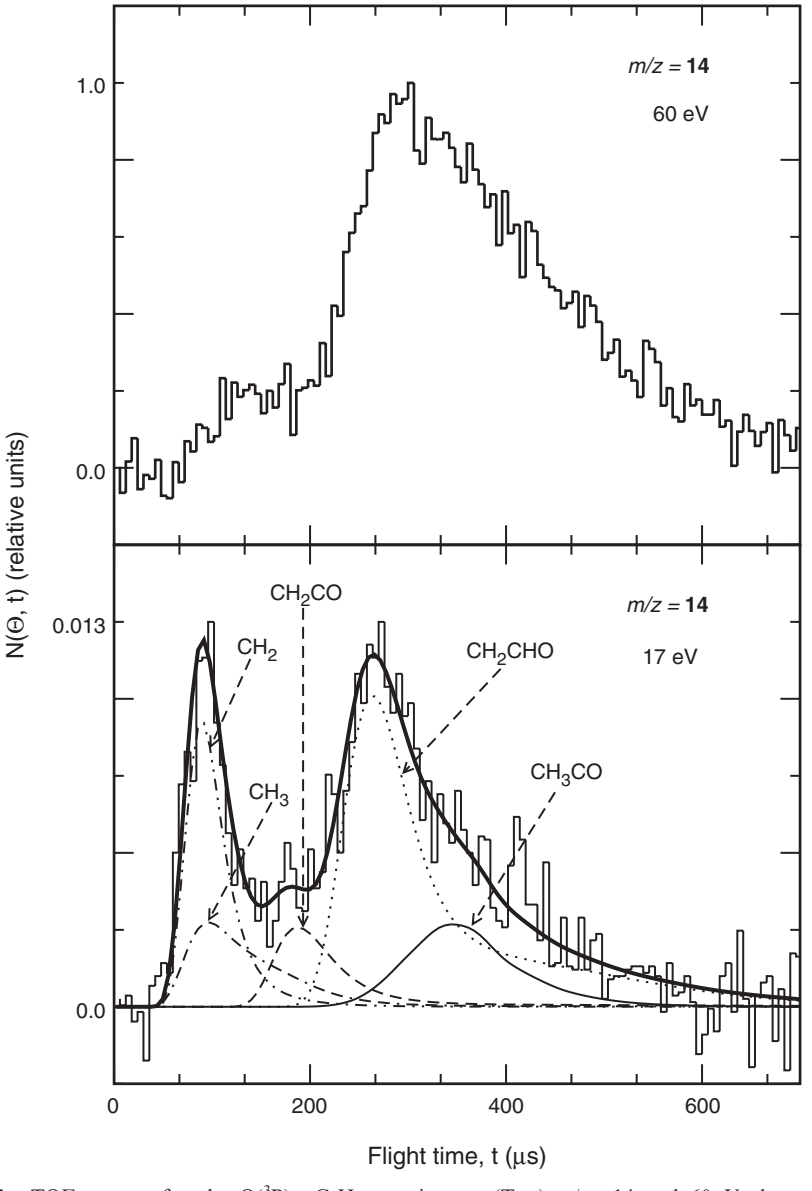

Figure 17. TOF spectra for the $O(^3P) + C_2H_4$ reaction at: (Top) $m/z = 14$ and 60 eV electron energy, reflecting C_2H_4 (detected at $m/z = 14$ as CH_2^+) elastically/inelastically scattered from O (slow peak) and undissociated O_2 (fast shoulder) contained in the oxygen beam; (Bottom) $m/z = 14$ and 17 eV electron energy, reflecting only reactive scattering signals since the elastic contribution has been completely suppressed (see text). Note the relative scale of the two spectra: the reactive signal at $m/z = 14$ (17 eV) is of the order of 1% of the elastic signal at $m/z = 14$ (60 eV). Note that all five detected channels contribute to the reactive signal at $m/z = 14$ (while the $CH_2 + H_2CO$ channel contributes through the parent ion of CH_2, all the other contribute via dissociative ionisation to CH_2^+, which is still present even at 17 eV electron energy). (Adapted from Ref. 77.)

ioniser of the vinoxy radical, corresponding to the $CH_2CHO + H$ channel (reaction 6a). The $m/z = 42$ TOF spectrum exhibits (i) a dominant peak, analogous to the main peak observed at $m/z = 15$, and which is due to dissociative ionisation in the ioniser of the vinoxy radical (reaction 6a), (ii) a fast peak, which appears as a shoulder on the main peak, which is unambiguously attributed, on the basis of energy and linear momentum conservation, to the ketene product from the channel $CH_2CO + H_2$ (reaction 6c), (iii) a small component, peaked at the CM velocity, which is attributed to formation of the acetyl radical from the channel $CH_3CO + H$ (reaction 6b) with a very small recoil energy. Note that the small peak of acetyl does not appear visible in the TOF spectrum at $m/z = 15$, presumably because of a different fragmentation pattern of hot vinoxy and hot acetyl. The $m/z = 14$ TOF spectrum exhibits contributions from fragmentation of the ketene, vinoxy, and acetyl products, and very clearly also a fast peak which can only correspond to methylene formation from the channel $CH_2 + HCHO$ (formaldehyde) (6e). A small contribution to this fast peak comes also from fragmentation of the CH_3 radical product from channel (6d), but this is small, considering that the appearance energy of CH_2^+ from CH_3 dissociative ionisation is AE = 15.1 eV [195]. We would like to stress that the detection of methylene from the reaction channel (6e) was only possible because of the use of soft EI. In fact, because the AE of CH_2^+ from C_2H_4 is 18 eV [195] by using an electron energy of 17 eV it was possible to remove completely the elastic contribution (which at 60 eV is about two orders of magnitude larger than the reactive signal – see top of figure 17) due to C_2H_4 scattered from the various components of the O-beam.

In this study [77, 196], it was found that formation of $CH_3 + HCO$ is the major channel (43%), followed by $CH_2CHO + H$ (27%); in addition, it was firmly established, for the first time, that formation of molecular products, $CH_2CO + H_2$, is a sizeable channel in the $O(^3P)$ + ethylene reaction, accounting for about 13% of the yield, conversely to what was concluded from the most recent and reliable kinetic studies [191]. For the first time, it was also shown that a small fraction (1%) of acetyl radicals is formed, and finally, we have observed unambiguously, under truly single collision conditions, formation of methylene + formaldehyde in the amount of 16%, corroborating two of the most recent kinetic investigations [190, 191].

Interestingly, these observations indicate that ISC plays an important role in the reaction, since the occurrence of channels (6b), (6c), and (6d), which account for about 2/3 of the overall reaction yield, can only be rationalised assuming that ISC between triplet and singlet PESs is occurring very efficiently. This is supported by recent theoretical work [186] using various QM methods and statistical rate theory on the PESs for both the triplet and singlet electronic states for the $O(^3P) + C_2H_4$ reaction. Product yields were found to be in excellent agreement with the branching ratio results derived from the CMB experiments, with the exception that the statistical theory underestimates the yield of the molecular channel leading to $CH_2CO + H_2$; however, this is not surprising considering that this channel is found to be highly non-statistical from our experiments [77, 196], with a $P(E_T')$ peaking at very high values ($\sim$165 kJ mol^{-1}) and reflecting a high exit potential barrier.

Dynamical calculations with inclusion of non-adiabatic couplings between the triplet and singlet PESs of C_2H_4O are desirable and would contribute to our understanding of the detailed, complex dynamics of this important reactive system.

4.4. *Reaction $C(^3P) + C_2H_4$*

As with the $O(^3P)$ reactions, also the reaction of C_2H_4 with $C(^3P)$ is significantly more complex than that with C_2H_2. In fact, it has many energetically allowed channels:

$$C(^3P) + C_2H_4(X^1A_g) \rightarrow [C_3H_4]^{\dagger} \rightarrow$$

$$\rightarrow H_2CCCH(X^2B_2) + H(^2S) \quad \Delta H_0^\circ = -188\,\text{kJ mol}^{-1} \quad (7a)$$

$$\rightarrow c\text{-}H_2CCCH(X^2A') + H(^2S) \quad \Delta H_0^\circ = -21\,\text{kJ mol}^{-1} \quad (7b)$$

$$\rightarrow c\text{-}HCCHCH(X^2A') + H(^2S) \quad \Delta H_0^\circ = -59\,\text{kJ mol}^{-1} \quad (7c)$$

$$\rightarrow H_3CCC(X^2A_1) + H(^2S) \quad \Delta H_0^\circ = -34\,\text{kJ mol}^{-1} \quad (7d)$$

$$\rightarrow HCCCH(^3B_1) + H_2(X^1\Sigma_g^+) \quad \Delta H_0^\circ = -213\,\text{kJ mol}^{-1} \quad (7e)$$

$$\rightarrow c\text{-}C_3H_2(X^1A^1) + H_2(X^1\Sigma_g^+) \quad \Delta H_0^\circ = -285\,\text{kJ mol}^{-1} \quad (7f)$$

$$\rightarrow C_2H_2(X^1\Sigma_g^+) + CH_2(X^3B^1) \quad \Delta H_0^\circ = -142\,\text{kJ mol}^{-1} \quad (7g)$$

$$\rightarrow C_2H(X_2\Sigma^+) + CH_3(X^2A^2) \quad \Delta H_0^\circ = -84\,\text{kJ mol}^{-1} \quad (7h)$$

Kinetic studies have found also this reaction very fast ($k_{298-15} = 2\text{–}4 \times 10^{-10}\,\text{cm}^3$ molecule^{-1} s^{-1}) down to very low temperatures [174, 175]. As far as product branching ratios are concerned, only a recent kinetic work at room temperature has determined the branching ratio for the H-forming channels to be $k_H/k_{total} = 0.92$ [182]. CMB experiments are again very valuable to provide information on the reaction dynamics and on the relative importance of the various possible products.

4.4.1. H-elimination channels. An early CMB study [197] at two E_c (17.2 and 38.5 kJ mol^{-1}) was able to identify only channel (7a), leading to propargyl + H formation, as the sole reaction pathway. A more recent, higher resolution CMB study in our laboratory [69], at three different E_c (9.1, 17.2, and 30.8 kJ mol^{-1}) was able to detect the formation of another C_3H_3 isomer, although it could not specify which of the three other energetically allowed ones (channels 7b, c, d). However, on the basis of theoretical information on the relevant PES [198], the best candidates were suggested to be *c*-propenyl (channel 7c) and propyn-1-yl (channel 7d). Figure 18 shows the angular distribution of the C_3H_3 products detected at $m/z = 38$ (because of better S/N than at $m/z = 39$) together with the Newton diagram of the experiment at $E_c = 30.8$ kJ mol^{-1}, while figure 19 shows an exemplary TOF spectrum recorded close to the CM angle. The corresponding distributions recorded at $m/z = 39$ (the parent peak of C_3H_3) were found [69] to be superimposable to those at $m/z = 38$, and this indicates unambiguously that the $m/z = 38$ signal is all coming from dissociative ionisation of the C_3H_3 product in the ioniser, and not from a dynamically different channel corresponding to H_2 elimination. Therefore, our study [69] was also able to show that the H_2 elimination channels

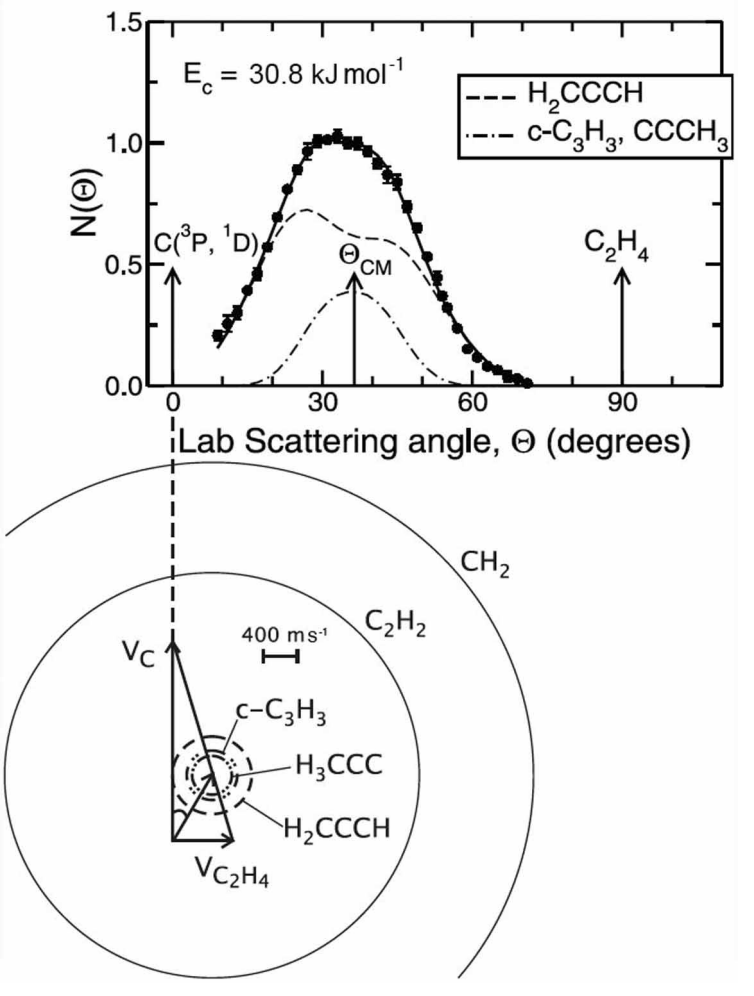

Figure 18. LAB angular distribution of the C_3H_3 products at $m/z = 38$ (solid circles) from the reaction $C(^3P) + C_2H_4$ at $E_c = 30.8\,kJ\,mol^{-1}$, together with the Newton diagram of the experiment. The circles in the diagram delimit the maximum velocity that the various, indicated C_3H_3 isomer products, and the C_2H_2 and CH_2 co-products from channel (7g), can attain on the basis of energy conservation if all the available energy goes into product translational energy. Solid line is the total angular distribution calculated from the best-fit product CM translational energy and angular distributions of the contributing channels, the distinct contributions from the propargyl (H_2CCCH) and the less stable C_3H_3 isomers being shown with dashed and dashed-dotted line, respectively. (Adapted from Ref. 69.)

(channels 7e and 7f) leading to *l*-$C_3H_2 + H_2$ and *c*-$C_3H_2 + H_2$, respectively, were not occurring to a measurable extent in the investigated collision energy range. As can be seen in figures 18 and 19, the angular and TOF distributions exhibit features attributable to formation of two energetically and also dynamically different C_3H_3 isomer products. This finding was fully supported by concurrent CMB experiments [69] in which the excitation function (i.e. the collision energy dependence of the integral cross-section) for H production was measured down to very low collision energies in

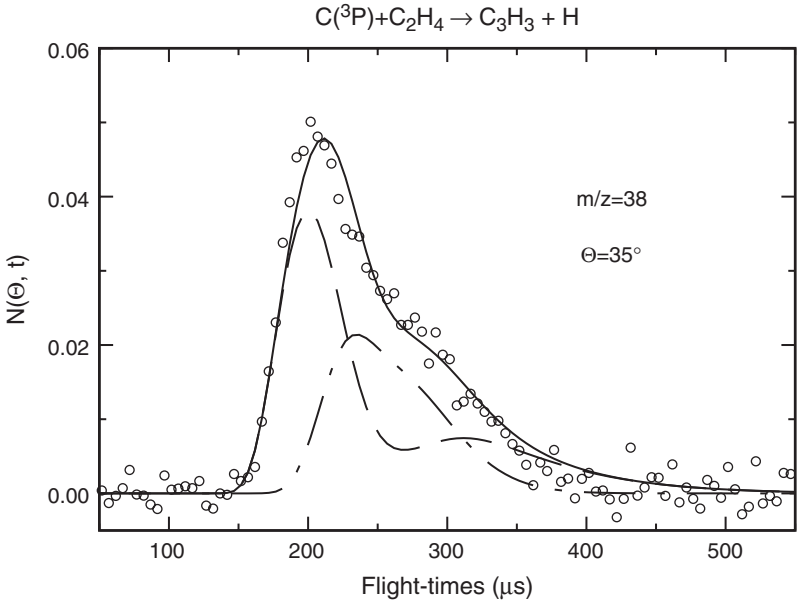

Figure 19. TOF distribution of the $m/z = 38$ products (open circles) from the $C(^3P) + C_2H_4$ reaction at $E_c = 30.8\,kJ\,mol^{-1}$ at the LAB angle of 35°. Symbols are as in figure 18.

CMB experiments with pulsed beams and LIF detection of the H-atoms; these experiments also gave evidence of the presence of two H-forming channels. Furthermore, our study [69] was also able to provide detailed information about the reaction dynamics of propargyl formation as a function of collision energy, giving also the branching ratio between formation of propargyl and the less stable C_3H_3 isomer(s). At the lowest E_c of $9.1\,kJ\,mol^{-1}$ formation of the less stable C_3H_3 isomer(s) is minor (2%), but it rises with increasing E_c to reach 14% at $E_c = 30.8\,kJ\,mol^{-1}$.

The results are in line with the kinetic branching ratio of 0.92 for H formation in $C(^3P) + C_2H_4$ [182], and with theoretical calculations [178, 198] which indicate that H_2 elimination from triplet propyne to $HCCCH(^3B_1) + H_2$ (channel 7e) has a very high energy barrier. H_2 could only be formed via ISC from triplet to singlet PESs with formation of $c\text{-}C_3H_2(^1A_1) + H_2$ (channel 7f). Our DCS results indicate that ISC in the C_3H_4 system is not an efficient process, as opposed to the C_3H_2 system. In this respect we note that the H-elimination channel is strongly exoergic for the $C(^3P) + C_2H_4$ system, while nearly thermoneutral for $C(^3P) + C_2H_2$; therefore, the C_3H_4 complex is likely to spend an amount of time in the triplet allene potential well (see figure 10c in ref. 66) significantly shorter than C_3H_2 does in the triplet propargylene (HCCCH) potential well (see figure 11) and this should determine a lower probability of ISC from the triplet to the singlet PES in C_3H_4.

However, our study with hard EI detection was not able to tell anything about the occurrence of the C–C bond breaking channel (7g) leading to formation of $C_2H_2 + CH_2$ (acetylene + methylene).

4.4.2. C–C bond fission channels. One reason for the difficulty in detecting the products of the C–C bond-rupture channels is due to the fact that two nearly equivalent fragments are produced in the process and, because of energy and linear momentum conservation, they are expected to be scattered over a wide angular range (see the Newton diagram in figure 18 where the maximum circles within which the two C_2H_2 and CH_2 co-products can be scattered are indicated). In addition, there is a severe complication which actually prevented the detection of the reactive scattering signal at $m/z = 26$ or 14. As mentioned in the Introduction, it is indeed impossible to detect any of the two products corresponding to the reaction pathway (7g) by using hard EI, because the reactive scattering signal at $m/z = 14$ (CH_2) or 26 (C_2H_2) is overwhelmed by the much more intense signal at these masses originating from dissociative ionization of elastically/inelastically scattered C_2H_4. This can be appreciated in figure 20 (top) which shows the TOF spectrum of $m/z = 14$ when using 60 eV electrons. This distribution is identical to that at $m/z = 28$ ($C_2H_4^+$), which clearly is due to elastically/inelastically scattered C_2H_4. Since the reactive scattering signal at $m/z = 14$ due to the formation of CH_2 (channel 7g) is expected to be about two order of magnitude smaller than the $m/z = 14$ signal coming from elastically scattered C_2H_4, there is no hope to be able to discern it. However, by using soft EI it has become possible to overcome this problem [192]. This is shown in the bottom of figure 20. In fact, since formation of CH_2^+ from C_2H_4 has an appearance energy AE = 18 eV [195], it is sufficient to lower the electron energy close to this value to suppress completely the elastic scattering contribution, and to reduce to zero any background at $m/z = 14$ due to dissociative ionisation of residual N_2. The TOF spectrum shown has been recorded by using 20 eV. As can be seen, the spectrum is very different from that shown in the top of figure 20: it exhibits a main, slow peak, and a fast shoulder. While the slow peak is due to dissociative ionisation to CH_2^+ of the main propargyl product (C_3H_3), the fast peak is readily attributed to methylene from the $CH_2 + C_2H_2$ channel. The observation of both product channels at the same $m/z = 14$ permits to determine the branching ratio. Finally, measurements at $m/z = 15$ using low electron energy should also be possible and reveal the possible occurrence of channel (7h) leading to $CH_3 + C_2H$. Such measurements are being planned.

Because of the acquired capability of measuring EI efficiency curves, it will also be possible and interesting to perform such measurements at $m/z = 39$, 38, 14, and 15. This should provide some information on the various C_3H_3 isomer products, since the IE of propargyl (CH_2CCH), cyclopropenyl (*c*-HCCHCH), and propyn-1-yl (CH_3CC) are quite different (8.7 eV, 6.6 eV, and 10.8 eV, respectively) [195]. Finally, because of the recently increased instrumental sensitivity, it should also be possible to revisit the H_2 forming channel, which may become detectable if larger than a few percent. This would permit to explore more deeply the possible occurrence of ISC in the C_3H_4 system.

5. Summary and outlook

In this review we have surveyed a significant amount of experimental results on the dynamics of both simple triatomic and complex polyatomic reactions, that have been obtained in our laboratory over the last few years by using the CMB

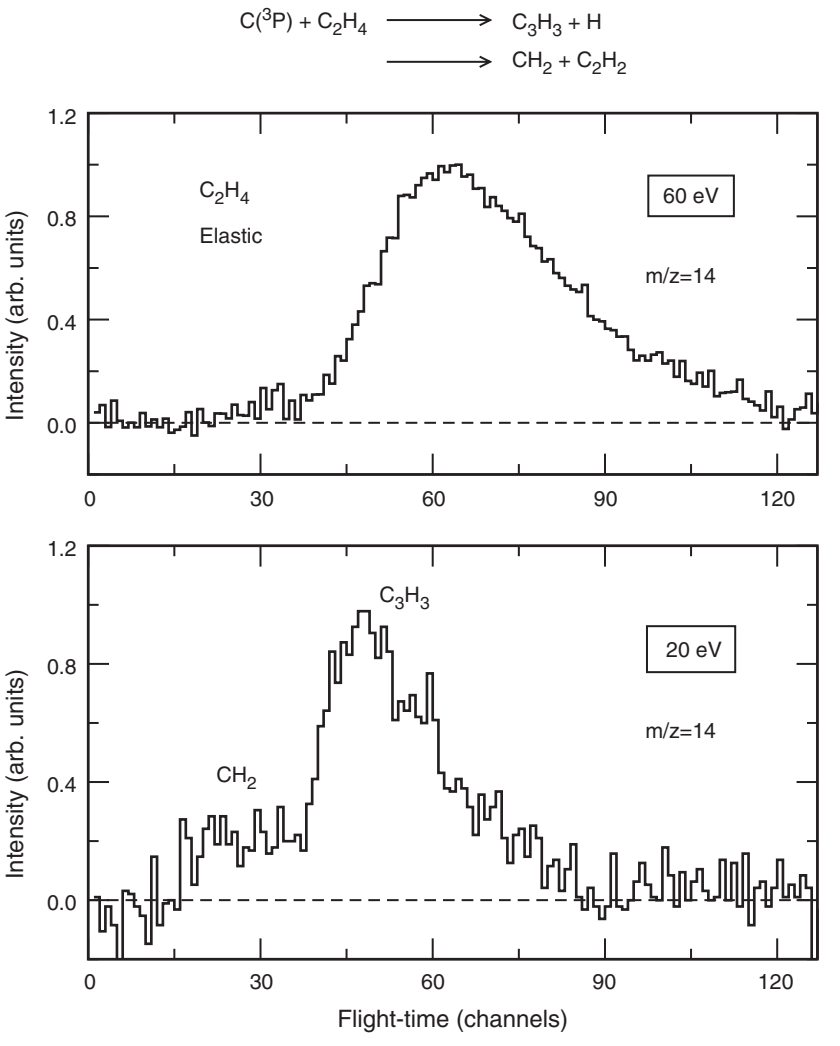

Figure 20. *Top panel*: TOF distributions (5 μs/channel) of $m/z = 14$ at $\Theta = 36^\circ$ and 60 eV electron energy from the reaction $C(^3P) + C_2H_4$ at $E_c = 30.8\,kJ\,mol^{-1}$. The $m/z = 14$ signal comes from dissociative ionisation of elastically/inelastically scattered C_2H_4. *Bottom panel*: TOF distribution of $m/z = 14$ at 20 eV electron energy; here the fast peak reflects CH_2 from channel (7g) while the slow peak reflects the C_3H_3 main product giving CH_2^+ via dissociative ionisation.

scattering technique. In particular, we have emphasised that a strong synergy between experiment and theory has been pivotal to the progress made in the understanding of prototypical triatom *insertion* reactions, while the implementation of soft EI for product detection has been central for progress in the investigation of the dynamics of polyatomic reactions exhibiting multiple channels.

More specifically, in the first part of the article, we have examined the current status of the comparisons between experiment (reactive differential cross-sections) and theory (exact QM and QCT scattering calculations on *ab initio* PESs, as well as QM statistical

calculations) for the prototypical *insertion* reactions $C(^1D) + H_2$, $N(^2D) + H_2$ and $O(^1D) + H_2$. These studies have involved a very close collaboration with theoretical groups, thus witnessing further that a strong interplay between experiment and theory is essential to the progress in the field of reaction dynamics. Although the agreement between experiment and theory is reasonably good in all cases, there is clearly still room for improvement regarding the accuracy of the *ab initio* PESs, as well as the inclusion of multisurface and non-adiabatic effects in QM scattering calculations. From the experimental point of view it is desirable that the $C(^1D) + H_2$ and $N(^2D) + H_2$ reactions be tackled by higher resolution techniques, able to provide state-resolved DCS, such as the H-Rydberg tagging method which is particularly suitable for these systems, as its application by Yang and co-workers [35] to the study of the $O(^1D) + H_2$ reaction has demonstrated. The main difficulty towards this may reside in the development of sufficiently intense and monoenergetic pulsed beams of $C(^1D)$ and $N(^2D)$ atoms, but we may reasonably expect that this will become feasible in the not too distant future. The comparison of theoretical predictions with state-resolved DCSs, when they become available, will allow a more detailed description of these systems. In the meantime, we can state that our knowledge, both experimental and theoretical, about the *insertion* reactions $O(^1D) + H_2$, $N(^2D) + H_2$ and $C(^1D) + H_2$ is approaching that achieved for the much more studied triatom abstraction reactions $H + H_2$, $F + H_2$ and $Cl + H_2$.

In the second part of the article we have reviewed the recent advances made in the investigation of polyatomic multichannel reactions. This is an area where new developments have been particularly challenging to make. A significant progress was made in our laboratory by the implementation of soft-ionisation with low-energy tunable electrons for product detection, and consequent reduction of interfering signal originating from dissociative ionisation. In addition, the implementation of a variable beam crossing angle set-up has also permitted extending the range of collision energies over which a given reaction can be studied. Exploiting these new features in an improved CMB instrument, we have elucidated the dynamics of practically important reactions, such as those of $O(^3P)$ and $C(^3P)$ with acetylene and ethylene, which are of significant relevance in combustion chemistry and astrochemistry.

Looking to the future, one may think to move to state-resolved experiments on these systems to gain further information on the dynamics. Unfortunately, there are fundamental limitations to obtaining quantum-state specific scattering data for polyatomic reactions, with the exception perhaps of reaction channels leading to products that can be probed very efficiently by REMPI, such as HCl [31, 64, 65] and CH_3 [21–27]. In any case, for polyatomic multichannel reactions the relevant issues are different with respect to those typical of simple triatomic reactions. The questions one needs to answer are: (i) What are the reaction channels actually occurring among the thermodynamically allowed ones? (ii) What is the nature of the primary products? (iii) What is the mechanism typical of each reaction channel? (iv) What is their relative yield? The answers to those questions will tell us, among other things, whether the reaction is proceeding statistically and whether non-adiabatic effects play a role. In this review we have illustrated that by using the CMB scattering technique with *universal* mass-spectrometric detection, featuring soft EI detection, it is possible to answer most of these questions: we can identify the primary products of practically all the competing reaction channels, characterise their dynamics and estimate their branching ratios over

an extended range of relative translational energies. Unfortunately, for polyatomic reactions it is not possible to perform rigorous quantum dynamical calculations on accurate multidimensional PESs. Direct dynamics QCT calculations on-the-fly in full dimensionality are perhaps the promising approach to treat theoretically the dynamics of polyatomic reactions. Such calculations are starting to be performed for reactions as $F + CH_4 \rightarrow HF + CH_3$ [200] and $Cl + RH \rightarrow HCl + R$ [64, 65]. Extensions of this approach to the multichannel reactions discussed in this review are around the corner [201–204]. In particular, advances in experiment and theory will make the reactions of $O(^3P)$ and $C(^3P)$ with C_2H_2 and C_2H_4 prototype reactions for detailed studies using the latest methods of reaction dynamics and related computational techniques.

We plan to use the same experimental approach in the future to tackle detailed dynamical studies of other reactions of practical relevance. Besides other reactions involving O and C atoms, we will explore reactions of N atoms and molecular radicals, such as OH and CN, or polyatomic radicals, such as alkyl radicals. Some reactions involving these atomic and radical species have been already investigated in our laboratory [66, 71, 72], but the novel capability of exploring all possible product channels is an incentive to re-investigate some of them. Another class of reactions we wish to investigate are those involving two open-shell reactants. Especially interesting are those radical–radical reactions, such as $N + OH$, $C + OH$ and $O + OH$, which are simple enough to be within the current theoretical capabilities. Another important class of radical–radical reactions are, for instance, those of $O(^3P)$ atoms with alkyl radicals which are of great relevance in combustion. In our laboratory we have recently developed a continuous supersonic beam source of hydrocarbon radicals and we have demonstrated that the dynamics of reactions such as $O(^3P) + CH_3$ and $O(^3P) + C_3H_5$ can be investigated in CMB experiments with mass spectrometric detection [205].

A more general conclusion is that such detailed studies on polyatomic reactions can contribute to bridge the gap between crossed-beam dynamics and thermal kinetics research by providing detailed information on the primary products and their branching ratios. In this direction, valuable contributions are also expected from CMB experiments with laser spectroscopic detection, possibly coupled to ion-imaging techniques [27–31], and with instruments using soft photo-ionisation by synchrotron VUV radiation [10, 78–81, 87–89]. The latter are expected to benefit greatly by the future implementation of VUV free electron laser sources, which should permit gaining significantly in VUV photon flux with respect to the current third generation synchrotron light sources, thus allowing for greater detection efficiency.

Acknowledgments

Special thanks go to Emeritus Professor G. G. Volpi for continuous inspiration and support over the years. We also thank past (M. Alagia, L. Cartechini) and present (R. Petrucci) group members, and visitors (A. Bergeat, R. Bobbenkamp) for their contribution to some aspects of the work discussed here. We wish to emphasize that a tight collaboration with the theoretical groups of Madrid (F. J. Aoiz and L. Bañares) and Rennes (J.-M. Launay and P. Honvault) has been central for the characterisation

of the dynamics of insertion reactions; many thanks go to all of them for the useful, fruitful and enjoyable collaboration on this topic. We acknowledge financial support from the Italian Ministero Istruzione, Università e Ricerca – MIUR (FIRB 2001 and PRIN 2005). This work is supported in part by the European Community's Human Potential Programme under Marie Curie Research Training Network 'MOLECULAR UNIVERSE' (contract MCRTN-CT-2004-512302) and Coordination Action 'EuroPlanet' (Contract 001637). Previous partial support from the EC Research Training Network 'REACTION DYNAMICS' (contract HPRN-CT-1999-00007) is also gratefully acknowledged.

It was a great pleasure and privilege to know Roger Miller since the beginning of both of our careers. Actually, it was Roger who asked me to write this review and so it is only right and gives me much pleasure to dedicate this work to him. I always enjoyed immensely to talk to my dear friend Roger at the very many conferences where we had the opportunity to meet. We always talked about science, but also about life, as we did for more than two hours during an excursion to the Chateau de Chillon (on the shore of lake Geneva) when I saw him for the last time in the occasion of the 28th International Symposium on Free Radicals held in Leysin, just one month and one half before this very sad event. I always had great admiration for his scientific achievements, his love for science, and his humanity. I personally will miss him a lot. His memory and example will always be with us.

References

[1] Y. T. Lee, in *Atomic and Molecular Beam Methods*, edited by G. Scoles (Oxford University Press, New York, 1987) Vol. 1, pp. 553–568.
[2] Y. T. Lee, Science **236,** 793 (1987).
[3] R. D. Levine and R. B. Bernstein, *Molecular Reaction Dynamics and Chemical Reactivity* (Oxford University Press, New York, 1987).
[4] R. D. Levine, *Molecular Reaction Dynamics* (Cambridge University Press, Cambridge, 2005).
[5] *Modern Trends in Chemical Reaction Dynamics: Experiment and Theory* (Part I & II); X. Yang and K. Liu, Eds., Adv. Series in Phys. Chem. Vol. 14 (World Scientific, Singapore, 2004).
[6] Y. T. Lee, J. D. McDonald, P. R. Le Breton, and D. R. Herschbach, Rev. Sci. Instrum. **40,** 1402 (1969).
[7] D. M. Neumark, A. M. Wodtke, G. N. Robinson, C. C. Hayden, and Y. T. Lee, J. Chem. Phys. **82,** 3045 (1985).
[8] M. Alagia, N. Balucani, P. Casavecchia, D. Stranges, and G. G. Volpi, J. Chem. Soc. Faraday Trans. **91,** 575 (1995).
[9] M. Faubel, B. Martinez-Haya, L. Y. Rusin, U. Tappe, and J. P. Toennies, J. Phys. Chem. A **101,** 6415 (1997).
[10] X. Yang, J. Lin, Y. T. Lee, D. A. Blank, A. G. Suits, and A. M. Wodtke, Rev. Sci. Instrum. **68,** 3317 (1997).
[11] J. J. Lin, S. Harich, Y. T. Lee, and X. Yang, Rev. Sci. Instrum. **69,** 1642 (1998).
[12] P. Casavecchia, G. Capozza and E. Segoloni, in *Modern Trends in Chemical Reaction Dynamics: Experiment and Theory (Part II)*; X. Yang and K. Liu, Eds., *Adv. Series in Phys. Chem.* Vol. 14 (World Scientific, Singapore, 2004), Ch. 7.
[13] J. J. Schroden and H. F. Davis, in *Modern Trends in Chemical Reaction Dynamics: Experiment and Theory (Part II)*; X. Yang and K. Liu, Eds., *Adv. Series in Phys. Chem.* Vol. 14 (World Scientific, Singapore, 2004), Ch. 5.
[14] P. Casavecchia, Rep. Progr. Phys. **63,** 355 (2000), and references therein.
[15] P. Casavecchia, N. Balucani, and G. G. Volpi, Annu. Rev. Phys. Chem. **50,** 347 (1999), and references therein.
[16] X. Yang, Phys. Chem. Chem. Phys. **8,** 205 (2006), and references therein.
[17] E. J. Murphy, J. H. Brophy, G. S. Arnold, W. L. Dimpfl, and J. L. Kinsey, J. Chem. Phys. **70,** 5910 (1979).
[18] D.-C., Che and K. Liu, Chem. Phys. **207,** 367 (1996).

[19] K. Liu, Annu. Rev. Phys. Chem. **52,** 139 (2001), and references therein.
[20] K. Liu, Int. Rev. Phys. Chem. **20,** 189 (2001).
[21] J. J. Lin, J. Zhou, W. Shiu, and K. Liu, Rev. Sci. Instrum. **74,** 2495 (2003).
[22] J. J. Lin, J. Zhou, W. Shiu, and K. Liu, Science **300,** 966 (2003).
[23] J. Zhou, J. J. Lin, W. Shiu, S.-C. Pu, and K. Liu, J. Chem. Phys. **119,** 2538 (2003).
[24] J. Zhou, J. J. Lin, W. Shiu, and K. Liu, J. Chem. Phys. **119,** 4997 (2003).
[25] B. Zhang, W. Shiu, and K. Liu, J. Phys. Chem. A **109,** 8993 (2005).
[26] B. Zhang, W. Shiu, and K. Liu, J. Phys. Chem. A **109,** 8989 (2005).
[27] K. Liu, in *Modern Trends in Chemical Reaction Dynamics: Experiment and Theory (Part II)*; X. Yang and K. Liu, Eds., *Adv. Series in Phys. Chem.* Vol. 14 (World Scientific, Singapore, 2004), Ch. 1.
[28] W. Li, C. Huang, M. Patel, D. Wilson, and A. G. Suits, J. Chem. Phys. **124,** 011102 (2006).
[29] D. Townsend, W. Li, S. K. Lee, R. L. Gross, and A. G. Suits, J. Phys. Chem. A **109,** 8661 (2005).
[30] A. J. R. Heck and D. W. Chandler, Annu. Rev. Phys. Chem. **46,** 335 (1995).
[31] M. N. R. Ashfold, N. H. Nahler, A. J. Orr-Ewing, O. P. J. Vieuxmaire, R. L. Toomes, T. N. Kitsopoulos, I. A. Garcia, D. A. Chestakov, S.-M. Wu, and D. H. Parker, Phys. Chem. Chem. Phys. **8,** 26 (2006), and references therein.
[32] L. Schnieder, K. Seekamp-Rahn, E. Wrede, and K. H. Welge, J. Chem. Phys. **107,** 6175 (1997).
[33] L. Schnieder *et al.*, Science **269,** 207 (1995).
[34] E. Wrede, L. Schnieder, K. H. Welge, F. J. Aoiz, L. Banares, J. F. Castillo, B. Martinez-Haya, and V. Herrero, J. Chem. Phys. **110,** 9971 (1999), and references therein.
[35] X. Yang, Int. Rev. Phys. Chem. **24,** 37 (2005), and references therein.
[36] X. Liu, J. J. Lin, S. A. Harich, G. C. Schatz, and X. Yang, Science **285,** 1249 (2000).
[37] B. R. Strazisar, C. Lin, and H. F. Davis, Science **290,** 958 (2000).
[38] S. A. Harich, D. Dai, C. C. Wang, X. Yang, S. D. Chao, and R. T. Skodjie, Nature **419,** 281 (2002).
[39] M. Alagia, N. Balucani, L. Cartechini, P. Casavecchia, E. H. van Kleef, G. G. Volpi, F. J. Aoiz, L. Bañares, D. W. Schwenke, T. C. Allison, S. L. Mielke, and D. G. Truhlar, Science, **273,** 1519 (1996).
[40] N. Balucani, D. Skouteris, L. Cartechini, G. Capozza, E. Segoloni, P. Casavecchia, M. H. Alexander, G. Capecchi, and H.-J. Werner, Phys. Rev. Lett. **91,** 013201 (2003).
[41] N. Balucani, D. Skouteris, G. Capozza, E. Segoloni, P. Casavecchia, M. H. Alexander, G. Capecchi, and H.-J. Werner, Phys. Chem. Chem. Phys. **6,** 5007 (2004).
[42] S.-H. Lee, L.-H. Lai, and K. Liu, J. Chem. Phys. **115,** 1197 (2001).
[43] S.-H. Lee, L.-H. Lai, and K. Liu, J. Chem. Phys. **110,** 8229 (1999).
[44] S.-H. Lee and K. Liu, J. Chem. Phys. **111,** 6253 (1999).
[45] F. Fernandez-Alonso and R. N. Zare, Annu. Rev. Phys. Chem. **53,** 67 (2002).
[46] S. C. Althorpe and D. C. Clary, Annu. Rev. Phys. Chem. **54,** 493 (2003).
[47] S. C. Althorpe, Int. Rev. Phys. Chem. **23,** 219 (2004).
[48] R. T. Skodje and X. Yang, Int. Rev. Phys. Chem. **23,** 253 (2004).
[49] M. Alagia, N. Balucani, P. Casavecchia, D. Stranges, G. G. Volpi, D. C. Clary,, A. Kliesch, and H.-J. Werner, Chem. Phys. **207,** 389 (1996).
[50] M. Alagia, N. Balucani, L. Cartechini, P. Casavecchia, E. H. van Kleef, G. G. Volpi, P. J. Kuntz, and J. J. Sloan, J. Chem. Phys. **108,** 6698 (1998).
[51] N. Balucani, P. Casavecchia, F. J. Aoiz, L. Bañares, J. F. Castillo, and V. J. Herrero, Mol. Phys. **103,** 1703 (2005).
[52] M. Alagia, N. Balucani, L. Cartechini, P. Casavecchia, G. G. Volpi, L. A. Pederson, G. C. Schatz, G. Lendvay, L. B. Harding, T. Hollebek, T.-H. Ho, and H. Rabitz, J. Chem. Phys. **110,** 8857 (1999).
[53] N. Balucani, M. Alagia, L. Cartechini, P. Casavecchia, G. G. Volpi, L. A. Pederson, and G. C. Schatz, J. Phys. Chem. A **105,** 2414 (2001).
[54] N. Balucani, L. Cartechini, G. Capozza, E. Segoloni, P. Casavecchia, G. G. Volpi, F. J. Aoiz, L. Bañares, P. Honvault and J.-M. Launay, Phys. Rev. Lett. **89,** 013201 (2002).
[55] N. Balucani, P. Casavecchia, L. Bañares, F. J. Aoiz, T. Gonzalez-Lezana, P. Honvault, and J.-M. Launay, J. Phys. Chem. A **110,** 817 (2006).
[56] A. Bergeat, L. Cartechini, N. Balucani, G. Capozza, L. Phillips, P. Casavecchia, G. G. Volpi, L. Bonnet, and J. C. Rayez, Chem. Phys. Lett. **327,** 197 (2000).
[57] N. Balucani, G. Capozza, L. Cartechini, A. Bergeat, R. Bobbenkamp, P. Casavecchia, F. J. Aoiz, L. Bañares, P. Honvault, B. Bussery-Honvault, and J.-M. Launay, Phys. Chem. Chem. Phys. **6,** 4957 (2004).
[58] N. Balucani, G. Capozza, E. Segoloni, A. Russo, R. Bobbenkamp, P. Casavecchia, T. Gonzalez-Lezana, E. J. Rackham, L. Bañares, and F. J. Aoiz, J. Chem. Phys. **122,** 234309 (2005).
[59] Y. T. Hsu, J.-H. Wang, and K. Liu, J. Chem. Phys. **107,** 2351 (1997).
[60] S.-H. Lee and K. Liu, J. Chem. Phys. **111,** 4351 (1999).
[61] S.-H. Lee and K. Liu, J. Phys. Chem. A **102,** 8637 (1998).
[62] S.-H. Lee and K. Liu, Chem. Phys. Lett. **290,** 323 (1998).

[63] S.-H. Lee and K. Liu, Appl. Phys. B **71,** 627 (2000).
[64] C. Murray and A. J. Orr-Ewing, Int. Rev. Phys. Chem. **23,** 435 (2004).
[65] see also: C. Murray, J. K. Pearce, S. Rudic, B. Retail, and A. J. Orr-Ewing, J. Phys. Chem. A **109,** 11093 (2005).
[66] P. Casavecchia, N. Balucani, L. Cartechini, G. Capozza, A. Bergeat, and G. G. Volpi, Faraday Discuss. **119,** 27 (2001).
[67] L. Cartechini, A. Bergeat, G. Capozza, P. Casavecchia, G. G. Volpi, W. D. Geppert, C. Naulin, and M. Costes, J. Chem. Phys. **116,** 5603 (2002).
[68] D. C. Clary, E. Buonomo, I. R. Sims, I. W. M. Smith, W. D. Geppert, C. Naulin, M. Costes, L. Cartechini, and P. Casavecchia, J. Phys. Chem. A **106,** 5541 (2002).
[69] W. D. Geppert, C. Naulin, M. Costes, G. Capozza, L. Cartechini, P. Casavecchia, and G. G. Volpi., J. Chem. Phys. **119,** 10607 (2003).
[70] N. Balucani, A. Bergeat, L. Cartechini, G. G. Volpi, and P. Casavecchia, in preparation.
[71] N. Balucani, M. Alagia, L. Cartechini, P. Casavecchia, G. G. Volpi, K. Sato, T. Takayanagi, and Y. Kurosaki, J. Am. Chem. Soc. **122,** 4443 (2000).
[72] N. Balucani, L. Cartechini, M. Alagia, P. Casavecchia, and G. G. Volpi, J. Phys. Chem. A **104,** 5655 (2000).
[73] N. Balucani, L. Cartechini, G. G. Volpi, and P. Casavecchia, in preparation.
[74] N. Balucani, D. Stranges, P. Casavecchia, and G. G. Volpi, J. Chem. Phys. **120,** 9571 (2004).
[75] M. Alagia, N. Balucani, L. Cartechini, P. Casavecchia, M. van Beek, and G. G. Volpi., Faraday Discuss. **113,** 133 (1999).
[76] G. Capozza, E. Segoloni, F. Leonori, G. G. Volpi, and P. Casavecchia, J. Chem. Phys. **120,** 4557 (2004).
[77] P. Casavecchia, G. Capozza, E. Segoloni, F. Leonori, N. Balucani, and G. G. Volpi, J. Phys. Chem. A **109,** 3527 (2005).
[78] C. C. Wang, J. Shu, J. J. Lin, Y. T. Lee, and X. Yang, J. Chem. Phys. **117,** 153 (2002).
[79] J. J. Lin, Y. Chen, Y. Y. Lee, Y. T. Lee, and X. Yang, Chem. Phys. Lett. **361,** 374 (2002).
[80] S.-H. Lee, Y.-Y. Lee, Y. T. Lee, and X. Yang, J. Chem. Phys. **119,** 827 (2003).
[81] S. H. Lee, J. J. Lin, and Y. T. Lee, J. Electr. Spectr. Rel. Phenom. **144–147,** 135 (2005).
[82] D. A. Blank, W. Sun, A. G. Suits, Y. T. Lee, S. W. North, and G. E. Hall, J. Chem. Phys. **108,** 5414 (1998).
[83] W. Sun, K. Yokoyama, J. C. Robinson, A. G. Suits, and D. M. Neumark, J. Chem. Phys. **110,** 4363 (1999); and references therein.
[84] J. A. Mueller, B. F. Parsons, L. J. Butler, F. Qi, O. Sorkhabi, and A. G. Suits, J. Chem. Phys. **114,** 4505 (2001).
[85] L. R. McCunn, K.-C. Lau, M. J. Krisch, L. Butler, J.-W. Tsung, and J. J. Lin, J. Phys. Chem. A **110,** 1625 (2006), and references therein.
[86] J. C. Robinson, S. A. Harris, W. Sun, N. E. Sveum, and D. M. Neumark, J. Am. Chem. Soc. **124,** 10211 (2002).
[87] D. A. Blank, N. Hemmi, A. G. Suits, and Y. T. Lee, Chem. Phys. **231,** 261 (1998).
[88] N. Hemmi and A. G. Suits, J. Chem. Phys. **109,** 5338 (1998).
[89] H. F. Davis, J. Shu, D. Peterka, and M. Ahmed, J. Chem. Phys. **121,** 6254 (2004).
[90] P. A. Willis, H. U. Stauffer, R. Z. Hinrichs, and H. F. Davis, Rev. Sci. Instrum. **70,** 2606 (1999).
[91] H. U. Stauffer, R. Z. Hinrichs, J. J. Schroden, and H. F. Davis, J. Chem. Phys. **111,** 10758 (1999).
[92] R. Z. Hinrichs, J. J. Schroden, and H. F. Davis, J. Am. Chem. Soc. **125,** 860 (2003), and references therein.
[93] W. L. Fitch and A. D. Sauter, Anal. Chem. **55,** 832 (1983).
[94] M. Costes, N. Daugey, C. Naulin, A. Bergeat, F. Leonori, E. Segoloni, R. Petrucci, N. Balucani, and P. Casavecchia, Faraday Discuss. **133** (2006), in press (DOI:10.1039/B518300F).
[95] M. Alagia, V. Aquilanti, D. Ascenzi, N. Balucani, D. Cappelletti, L. Cartechini, P. Casavecchia, F. Pirani, G. Sanchini, and G. G. Volpi, Isr. J. Chem. **37,** 329 (1997).
[96] S. J. Sibener, R. J. Buss, C. Y. Ng, and Y. T. Lee, Rev. Sci. Instrum. **51,** 167 (1980).
[97] F. J. Aoiz, L. Bañares, and V. J. Herrero, Int. Rev. Phys. Chem. **24,** 119 (2005).
[98] Dong, S.-H. Lee, and K. Liu, J. Chem. Phys. **113,** 3633 (2000); R. T. Skodjie, D. Skouteris, D. E. Manolopoulos, S.-H. Lee, F. Dong, and K. Liu, Phys. Rev. Lett. **85,** 1206 (2000).
[99] M. H. Alexander, D. E. Manolopoulos, and H.-J. Werner, J. Chem. Phys. **113,** 11084 (2000); Y.-R. Tzeng and M. H. Alexander, Phys. Chem. Chem. Phys. **6,** 5018 (2004).
[100] Y. S. M. Wu and A. Kuppermann, Chem. Phys. Lett. **235,** 105 (1995).
[101] L. A. Pederson, G. C. Schatz, T.-S. Ho, T. Hollebeek, H. Rabitz, L. B. Harding, and G. R. Lendvay, J. Chem. Phys. **110,** 9091 (1999).
[102] L. A. Pederson, G. C. Schatz, T.-S. Ho, T. Hollebeek, H. Rabitz, and L. B. Harding, J. Phys. Chem. A **104,** 2301 (2000).

[103] T.-S. Ho, H. Rabitz, F. J. Aoiz, L. Bañares, S. A. Vázquez, and L. B. Harding, J. Chem. Phys. **119,** 3063 (2003).
[104] A. J. Dobbyn and P. J. Knowles, Mol. Phys. **91,** 1107 (1997).
[105] B. Bussery-Honvault, P. Honvault, and J.-M. Launay, J. Chem. Phys. **115,** 10701 (2001).
[106] L. Bañares, F. J. Aoiz, S. A. Vázquez, T.-S. Ho, and H. Rabitz, Chem. Phys. Lett. **374,** 243 (2003).
[107] A. S. Zyubin, A. M. Mebel, S. D. Chao, and R. T. Skodje, J. Chem. Phys. **114,** 320 (2001).
[108] T.-S. Ho, T. Hollebeek, H. Rabitz, S. D. Chao, R. T. Skodje, A. S. Zyubin, and A. M. Mebel, J. Chem. Phys. **116,** 4124 (2002).
[109] E. J. Rackham, F. Huarte-Larranaga, and D. E. Manolopoulos, Chem. Phys. Lett. **343,** 356 (2001).
[110] E. J. Rackham, T. Gonzalez-Lezana, and D. E. Manolopoulos, J. Chem. Phys. **119,** 12895 (2003).
[111] D. C. Clary and J. P. Henshaw, Faraday Discuss. Chem. Soc. **84,** 333 (1987).
[112] S. Y. Lin and H. Guo, J. Chem. Phys. 120, 9907 (2004).
[113] S. Y. Lin and H. Guo, J. Phys. Chem. A **108,** 10066 (2004).
[114] M. Alagia, N. Balucani, L. Cartechini, P. Casavecchia, E. H. van Kleef, G. G. Volpi, P. J. Kuntz, and J. J. Sloan, Faraday Discuss. **108,** 430 (1997).
[115] P. Honvault and J.-M. Launay, J. Chem. Phys. **111,** 6665 (1999).
[116] P. Honvault and J.-M. Launay, J. Chem. Phys. **114,** 1057 (2001).
[117] L. Bañares, F. J. Aoiz, P. Honvault, B. Bussery-Honvault, and J.-M. Launay, J. Chem. Phys. **118,** 565 (2003).
[118] F. J. Aoiz, L. Bañares, J. F. Castillo, V. J. Herrero, B. Martinez-Haya, P. Honvault, J.-M. Launay, X. H. Liu, J. J. Lin, S. Harich, C. C. Wang, and X. Yang, J. Chem. Phys. **116,** 10692 (2002).
[119] F. J. Aoiz, L. Bañares, J. F. Castillo, M. Brouard, W. Denzer, C. Vallance, P. Honvault and J.-M. Launay, Phys. Rev. Lett. **86,** 1729 (2001).
[120] J. E. Pollard, D. J. Trevor, Y. T. Lee, and D. A. Shirley, J. Chem. Phys. **77,** 4818 (1982).
[121] B. Bussery-Honvault, J. Julien, P. Honvault, and J.-M. Launay, Phys. Chem. Chem. Phys. **7,** 1476 (2005).
[122] A. R. W. McKellar, P. R. Bunker, T. J. Sears, K. M. Evenson, R. J. Saykally and S. R. Langhoff, J. Chem. Phys. **79,** 5251 (1983).
[123] H. Petek, D. J. Nesbitt, D. C. Darwin and C. B. Moore, J. Chem. Phys. **86,** 1172 (1987).
[124] H. Petek, D. J. Nesbitt, C. B. Moore, F. W. Birss and D. A. Ramsay, J. Chem. Phys. **86,** 1189 (1987).
[125] H. Petek, D. J. Nesbitt, D. C. Darwin, P. R. Ogilby and C. B. Moore, J. Chem. Phys. **91,** 6566 (1981).
[126] J. F. Castillo, D. E. Manolopoulos, K. Stark, and H.-J. Werner, J. Chem. Phys. **104,** 6531 (1996).
[127] F. Santoro, C. Petrongolo, and G. C. Schatz, J. Phys. Chem. A **106,** 8276 (2002).
[128] T.-S. Ho, T. Hollebeck, H. Rabitz, L. B. Harding, and G. C. Schatz, J. Chem. Phys. **105,** 10472 (1996).
[129] G. C. Schatz, A. Papaioannou, L. A. Pederson, L. B. Harding, T. T. Hollebeck, T.-S. Ho, and H. Rabitz, J. Chem. Phys. **107,** 2340 (1997).
[130] X. H. Liu, J. J. Lin, S. Harich, and X. Yang, Phys. Rev. Lett. **86,** 408 (2001).
[131] X. H. Liu, J. J. Lin, S. Harich, and X. Yang, J. Chem. Phys. **113,** 1325 (2000).
[132] X. H. Liu, C. C. Wang, S. Harich, and X. Yang, Phys. Rev. Lett. **89,** Art. No. 133201 (2002).
[133] P. Hermine, Y. T. Hsu, and K. Liu, Phys. Chem. Chem. Phys. **2,** 581 (2000).
[134] Y.-T. Hsu and K. Liu, J. Chem. Phys. **107,** 1664 (1997).
[135] D. C. Che and K. Liu, J. Chem. Phys. **103,** 5164 (1995).
[136] M. Ahmed, D. S. Peterka, and A. G. Suits, Chem. Phys. Lett. **301,** 372 (1999).
[137] P. M. Aker and J. J. Sloan, J. Chem. Phys., 85, 1412 (1986).
[138] C. B. Cleveland, G. M. Jurisch, M. Trolier, and J. R. Wiesenfeld, J. Chem. Phys. **86,** 3253 (1987).
[139] K. Mikulecky and K.-H. Gericke, Chem. Phys. **175,** 13 (1993).
[140] A. J. Alexander, F. J. Aoiz, M. Brouard, and J. P. Simons, Chem. Phys. Lett., **256,** 561 (1996).
[141] A. J. Alexander, D. A. Blunt, M. Brouard, J. P. Simons, F. J. Aoiz, L. Bañares, Y. Fujimura, and M. Tsubouchi, Faraday Discuss. **108,** 375 (1997).
[142] A. J. Alexander, F. J. Aoiz, L. Bañares, M. Brouard, J. Short, and J. P. Simons, J. Phys. Chem. A **101,** 7544 (1997).
[143] S. K. Gray, G. G. Balint-Kurti, G. C. Schatz, J. J. Lin, X. H. Liu, S. Harich, and X. Yang, J. Chem. Phys. **113,** 7330 (2000).
[144] Y. T. Hsu, K. Liu, L. A. Pederson, and G. C. Schatz, J. Chem. Phys. **111,** 7921 (1999).
[145] Y. T. Hsu, K. Liu, L. A. Pederson, and G. C. Schatz, J. Chem. Phys. **111,** 7931 (1999).
[146] R. J. Buss, P. Casavecchia, T. Hirooka, S. J. Sibener, and Y. T. Lee, Chem. Phys. Lett. **82,** 386 (1981).
[147] P. J. Kuntz, B. I. Niefer, J. J. Sloan, Chem. Phys. **151,** 77 (1991).
[148] P. A. Berg, P. J. Kuntz, J. Chem. Phys., **95,** 8038 (1991).
[149] P. J. Kuntz, B. I. Niefer, and J. J. Sloan, J. Chem. Phys. **88,** 3629 (1998).
[150] R. Polák, K. Paiderová, P. J. Kuntz, J. Chem. Phys. **87,** 2863 (1987).

[151] M. Hankel, G. G. Balint-Kurti, and S. K. Gray, J. Phys. Chem. A **105,** 2330 (2001).
[152] K. Drukker and G. C. Schatz, J. Chem. Phys. **111,** 2451 (1999).
[153] S. K. Gray, C. Petrongolo, K. Drukker, and G. C. Schatz, J. Phys. Chem. A **103,** 948 (1999).
[154] F. J. Aoiz, L. Bañares, M. Brouard, J. F. Castillo, and V. J. Herrero, J. Chem. Phys. **111,** 5339 (2000).
[155] F. J. Aoiz, L. Bañares, J. F. Castillo, B. Martínez-Haya, and M. P. Miranda, J. Chem. Phys. **114,** 8328 (2001).
[156] F. J. Aoiz, L. Bañares, J. F. Castillo, J. F. Herrero, and B. Martínez-Haya, Phys. Chem. Chem. Phys. **4,** 4379 (2002).
[157] J. Brandão and C. M. A. Rio, Chem. Phys. Lett. **372,** 866 (2003).
[158] J. Brandão and C. M. A. Rio, Chem. Phys. Lett. **377,** 523 (2003).
[159] J. Brandão and C. M. A. Rio, J. Chem. Phys. **119,** 3148 (2003).
[160] S. Y. Lin and H. Guo, Chem. Phys. Lett. **385,** 193 (2004).
[161] M. H. Alexander, E. J. Rackham, and D. E. Manolopoulos, J. Chem. Phys. **121,** 5221 (2004).
[162] D. J. Hucknall, *Chemistry of Hydrocarbon Combustion* (Chapman Hall, New York, 1985), p. 199.
[163] D. L. Baulch, C. J. Cobos, R. A. Cox, P. Frank, G. Hayman, Th. Just, J. A. Kerr, T. Murrels, M. J. Pilling, J. Troe, R. W. Walker, and J. Warnatz, J. Phys. Chem. Ref. Data **23,** 847 (1994); and references therein.
[164] A. M. Schmoltner, P. M. Chu, and Y. T. Lee, J. Chem. Phys. **91,** 5365 (1989).
[165] J. Peeters, W. Boullart, and I. Langhans, Int. J. Chem. Kinet. **26,** 869 (1994).
[166] W. Boullart and J. Peeters, J. Phys. Chem. **96,** 9810 (1992).
[167] L. B. Harding and A. F. Wagner, J. Phys. Chem. **90,** 2974 (1986).
[168] J. V. Michael and A. F. Wagner, J. Phys. Chem. A **94,** 2453 (1990).
[169] D. R. Yarkony, J. Phys. Chem. A **102,** 5305 (1998).
[170] A. R. Clemo, G. L. Duncan, and R. Grice, J. Chem. Soc. Faraday Trans. 2 **78,** 1231 (1982).
[171] F. Leonori, G. Capozza, E. Segoloni, N. Balucani, G. G. Volpi and P. Casavecchia, in preparation.
[172] C. C. Hayden, D. M. Neumark, K. Shobatake, R. K. Sparks, and Y. T. Lee, J. Chem. Phys. **76,** 3607 (1982).
[173] C. Ochsenfeld, R. I. Kaiser, Y. T. Lee, A. G. Suits, and M. Head-Gordon, J. Chem. Phys. **106,** 4141 (1997).
[174] D. Chastaing, P. L. James, I. R. Sims and I. W. M. Smith, Phys. Chem. Chem. Phys. **1,** 2247 (1999).
[175] D. Chastaing, S. D. Le Picard, I. R. Sims and I. W. M. Smith, Astron. Astrophys. **365,** 241 (2001).
[176] R. I. Kaiser, C. Ochsenfeld, M. Head-Gordon, Y. T. Lee, and A. G. Suits, J. Chem. Phys. **106,** 1729 (1997).
[177] J. Takahashi and K. Yashimata, J. Chem. Phys. **104,** 6613 (1996).
[178] A. M. Mebel, W. M. Jackson, A. H. H. Chang, and S. H. Lin, J. Am. Chem. Soc. **120,** 5751 (1998).
[179] R. Guadagnini, G. C. Schatz, and S. P. Walch, J. Phys. Chem. A **102,** 5857 (1998).
[180] E. Buonomo and D. C. Clary, J. Phys. Chem. A **105,** 2694 (2001).
[181] T. Takayanagi, Chem. Phys. **312,** 61 (2005); J. Phys. Chem. A **110,** 361 (2006).
[182] A. Bergeat and J.-C. Loison, Phys. Chem. Chem. Phys. **3,** 2038 (2001).
[183] F. Leonori, E. Segoloni, R. Petrucci, A. Bergeat, N. Balucani, and P. Casavecchia, to be published.
[184] B. E. Turner, E. Herbst, and R. Terzevia, Astrophys. J. Suppl. Ser. **126,** 427 (2000).
[185] D. Fossé, J. Cernicharo, M. Gerin, and P. Cox, Astrophys. J. **552,** 168 (2001).
[186] T. L. Nguyen, L. Vereecken, H. J. Hou, M. T. Nguyen, and J. Peeters, J. Phys. Chem. A **109,** 7489 (2005).
[187] A. M. Schmoltner, P. M. Chu, R. J. Brudzynski, and Y. T. Lee, J. Chem. Phys. **91,** 6926 (1989).
[188] K. Brezinsky, Prog. Energy Combust. Sci. **12,** 1 (1986).
[189] R. J. Cvetanović and D. L. Singleton, Reviews Chem. Int. **5,** 183 (1984); and references therein.
[190] Y. Endo, S. Tsuchiya, C. Yamada, E. Hirota, and S. Koda, J. Chem. Phys. **85,** 4446 (1986).
[191] U. Bley, P. Dransfeld, B. Himme, M. Koch, F. Temps, and H. Gg. Wagner, *Twenty-Second Symposium (International) on Combustion* (The Combustion Institute, Pittsburgh, 1988), p. 997.
[192] K. Yamaguchi, S, Yabushita, T. Fueno, S. Kato, and K. Morokuma, Chem. Phys. Lett. **70,** 27 (1980).
[193] M. Dupuis, J. J. Wendoloski, T. Takada, and W. A. Lester Jr, J. Chem. Phys. **76,** 481 (1982).
[194] R. J. Buss, R. J. Baseman, G. He, and Y. T. Lee, J. Photochem. **17,** 389 (1981).
[195] NIST Chemistry WebBook, 2002.
[196] P. Casavecchia *et al*, in preparation.
[197] R. I. Kaiser, Y. T. Lee, and A. G. Suits, J. Chem. Phys. **105,** 8705 (1996).
[198] T. N. Le, H.-Y. Lee, A. M. Mebel, and R. I. Kaiser, J. Phys. Chem. A **105,** 1847 (2001).
[199] P. Casavecchia *et al*., work in progress.
[200] J. F. Castillo, F. J. Aoiz, L. Bañares, E. Martinez-Nuñez, A. Fernández-Ramos, and S. Vazquez, J. Phys. Chem. A **109,** 8459 (2005).
[201] W. L. Hase, personal communication.
[202] J. M. Bowman, personal communication.

[203] G. C. Schatz, personal communication.
[204] F. J. Aoiz, personal communication.
[205] F. Leonori, E. Segoloni, N. Balucani, R. Petrucci, A. Bergeat, D. Stranges, and P. Casavecchia, Proceedings of 28th International Symposium on Free Radicals (Leysin, Switzerland, 4-9 September 2005), p. 116; and in preparation.